Nanoscale 10.27 (2018): 12935-12956

DOI: http://dx.doi.org/10.1039/c8nr02307g

Received 00th January 20xx,
Accepted 00th January 20xx

DOI: 10.1039/x0xx00000x

www.rsc.org/

Fluorescence Imaging Group, Departamento de Física de Materiales, Facultad de Ciencias, Universidad Autónoma de Madrid, C/ Francisco Tomás y Valiente 7, 28049, Madrid, Spain.
Grupo de Nano-Fotônica e Imagens, Instituto de Física, Universidade Federal de Alagoas, 57072-900, Maceió-AL, Brazil.
Instituto Ramón y Cajal de Investigación Sanitaria IRYCIS, Ctra. Colmenar km. 9.100 Madrid, 28034, Spain.
Departamento de Física Aplicada, Facultad de Ciencias, Universidad Autónoma de Madrid, C/ Francisco Tomás y Valiente 7, 28049, Madrid, Spain.
† Footnotes relating to the title and/or authors should appear here.
Electronic Supplementary Information (ESI) available: [details of any supplementary information available should be included here]. See DOI: 10.1039/x0xx00000x

Core-shell rare-earth-doped nanostructures in biomedicine

Lucia Labrador-Páez,[a] Erving C. Ximendes,[b] Paloma Rodríguez-Sevilla,[a] Dirk H. Ortgies,[a,c] Ueslen Rocha,[b] Carlos Jacinto,[b] Emma Martín Rodríguez,[c,d] Patricia Haro-González,[a] and Daniel Jaque*,[a,c]

The current status of the use of core-shell rare-earth-doped nanoparticles for biomedical applications is reviewed in detail. The different core-shell rare-earth-doped nanoparticles developed so far are described and the most relevant examples of their application for imaging, sensing, and therapy are summarized. In addition, the advantages and disadvantages they present are discussed. Finally, a critical opinion of their potential application in real life biomedicine is given.

A. Introduction

The battle against diseases is continuously bringing new challenges that can only be overcome if faced from a multidisciplinary standpoint and by taking advantage of the synergies between very different but complementary research areas such as biology, medicine, physics, chemistry, and mathematics. Among the current different multidisciplinary research lines, aimed to face the challenges posed by those illnesses that are the major causes of mortality (such as cancer or cardiovascular diseases), those focused on the development of new materials and techniques that would improve diagnosis and therapy are attracting the greatest attention. These research lines have three main objectives. Firstly, the achievement of earlier diagnosis in order to improve the success rate of posterior treatments. Secondly, the reduction of "collateral damages" and side effects caused by current therapies. Finally, the development of cost-effective diagnosis and therapy procedures that result in a wider distribution of health coverage and sustainable health systems. In this sense, nanotechnology is playing a central role as it is leading to the continuous appearance of new materials and techniques. In particular, during the last few years, the refinement of nanofabrication processes has led to a large variety of nanosized materials with pre-tailored properties and potential application as biocompatible markers, drug deliverers, and therapeutic agents. Indeed, the synergy between nanotechnology and medicine has led to the appearance of a new research area commonly called nanomedicine.[1, 2] Its fundamental purpose is the use of nanoparticles (NPs, with sizes below 100 nm) as diagnostic and therapeutic agents. The reduced size of NPs together with adequate surface functionalization make their colloidal stability in fluids, including blood, possible.[3] They could present a large *in vivo* circulation time with improved bioavailability. This allows whole body distribution of the NPs for imaging applications or, through specific surface chemistry, the targeting of tumours or cardiovascular lesions, for example.[4, 5]

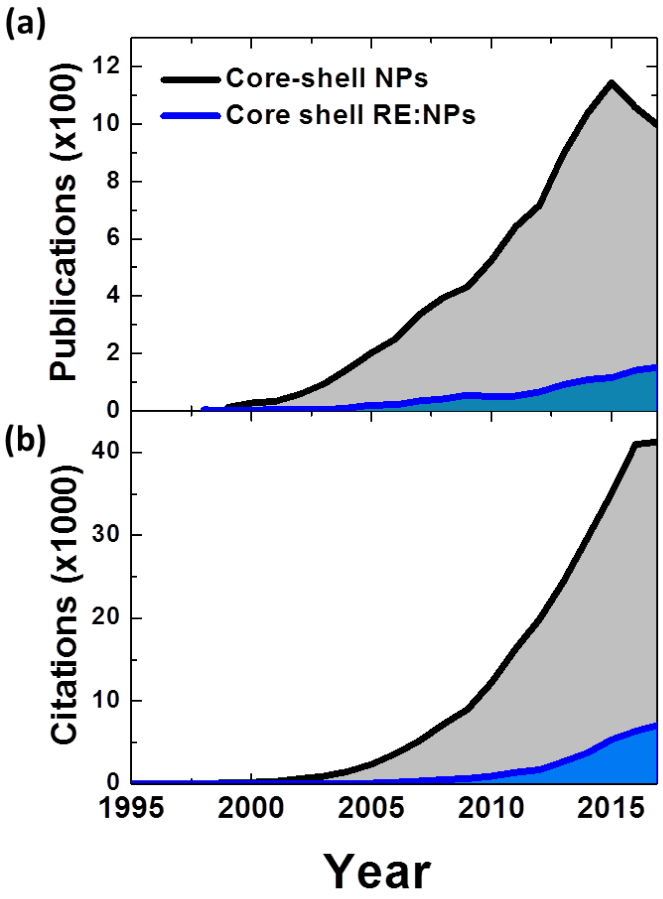

Figure 1. (a) Publications and (b) citations of scientific papers on CS NPs (black) and on CS RENPs (blue) per year since 1995. Data from the Web of Science, Thomson Reuters.

Luminescent NPs (LNPs) are one of the most popular NPs for the scientific community working in nanomedicine. They employ light either as trigger stimulus or as imaging signal. In comparison with other NPs used as diagnostic or therapeutic agents (such as magnetic NPs), LNPs have the advantage of requiring cost-effective and portable excitation sources such as near-infrared (NIR) laser diodes. Therefore, the use of LNPs in nanomedicine is a fast-developing research field. It was initially boosted by the use of visible (VIS) emitting quantum dots, dyes, and proteins[6, 7]. Each one of these pioneering systems has its own limitations, in most of the cases, regarding toxicity, long-term instability, and poor penetration into tissues. These drawbacks motivated the research on alternative systems such as rare-earth-doped NPs (RENPs), which were introduced almost 20 years ago.[8] The advantages of RENPs are their low toxicity, outstanding long-term stability, narrow emission lines, and the possibility of tuning their working spectral ranges by adequate doping.[9-11] The first RENPs developed for nanomedicine presented a very simple architecture. They were constituted by a core surrounded by a variable surface decoration that provided the RENPs with colloidal stability and, in some cases, with targeting abilities. This simple NP architecture soon evidenced some limitations. The first one was the poor isolation of rare-earth (RE) ions at the surface from the environment, which led to a drastic reduction in the luminescence efficiency (due to the increment of non-radiative processes).[12] The second limitation that researchers found when working with single-core RENPs was the difficulty of improving their multifunctionality. First attempts to develop single-core multifunctional RENPs were

done by introducing several RE ions in the core.[13] Unfortunately, this strategy often failed as the presence of different RE ions in close proximity leads to the appearance of undesirable energy transfer-assisted luminescence quenching. Thus, a new strategy was required to simultaneously provide RENPs with multifunctionality while keeping at minimum undesirable interactions with molecules in the environment.

Core-shell (CS) engineering then emerged as a very convenient solution. CS engineering consists in the controlled growth of a protective shell around the original core RENP. Since the very first development of CS NPs, the scientific community realized that it was a powerful approach leading to new nanostructures with improved properties.[14] A simple bibliographic research evidences this fact. Figure 1a shows the historic evolution of the number of scientific papers dealing with "core-shell nanoparticles". As it can be observed, from 1996 up to now the number of published papers shows a steady growth. Most of the early published papers dealt with metallic (gold) NPs. In that case the interest of adopting CS structures was due to the possibility of achieving full control over their plasmonic resonance.[15] From that moment CS engineering spreads to different fields. For instance, one of the pioneering works published in 1996 proposed the use of CS nanostructures for hydrogen storage.[16] In 1998, it was already possible to find papers demonstrating the ability of CS engineering to improve the luminescent properties of LNPs, for example, how CS arrangement could significantly reduce photodegradation in the widely used CdSe Quantum Dots.[17] This work was of special relevance for the expanding community working on LNPs for biomedical applications, as it demonstrated that such structures can be improved significantly by just adding one or two steps in their synthesis procedure. This interest was further boosted in 2005, when reports on the minimal toxicity that CS NPs could have in *in vivo* studies were published.[18] This could explain the fast increment of citations taking place after this year. The fascination caused by CS structures affected not only the researchers working on metallic or semiconductor NPs, but also it influenced the scientific community working on RENPs. They directly realized that adopting CS structures could be a solution to the limitations impeding the real application of RENPs in biomedicine. One of the first works reporting on CS nanostructures containing RE ions was published in 2004 by Lu *et al*.[19] These authors were able to grow an erbium and ytterbium-doped shell over a magnetic NP, resulting in a multifunctional nanostructure. At the end of the same year, Van Veggel´s group demonstrated the benefits of adding an inert shell to increase the brightness of RENPs.[20] Some years later, in 2008, DiMaio *et al.*[21] demonstrated the possibility of tailoring the spectroscopic properties of RENPs by controlling the energy transfer between multiple rare-earth dopants. Such control was achieved by means of an adequate combination of complex CS engineering and selective RE doping of the different layers.[21] Just one year later, Vetrone, at Capobianco´s group, published a reference work introducing the "active-core/active-shell" concept and demonstrated how this can be used to drastically improve the brightness of upconverting (UC) RENP.[14] From the analysis of the bibliographic data included in Figure 1, it is clear, specially looking at the time evolution of citations, that the publication of these last works constituted a milestone. The message sent to the scientific community was that it was worth working on the design and development of CS RENPs since this will be the route to eventually apply them to nanomedicine.

At this moment, more than 10 years after the publication of these key works, the number of citations received by studies dealing with CS RENPs is still growing (see Figure 1b). Nevertheless, a slight deceleration in both the number of citations and number of publications is observed. There is no clear explanation for this fact. In our opinion, the effort over the last years have been focused on the synthesis of improved structures and the design and development of proof-of-concept demonstrations. Thus, the next big step is to bring the developed structures to the clinic and industrial applications. This will require a careful analysis of the achievements in the field and its potential directions, identifying the remaining challenges and their possible solutions. This review is aimed to contribute towards this process. The most relevant achievements regarding the potential application of CS RENPs in nanomedicine are herein summarized, starting with a brief description of the most commonly used routes for synthesis of CS RENPs (Section B), followed by their possible application in bioimaging (Section C), sensing (Section D), and therapy (Section E). The advantages and drawbacks of CS RENPs and a critical opinion about their applicability in clinical medicine are finally given in Section F.

B. ROUTES FOR THE SYNTHESIS

Many examples can be found in the literature describing the preparation of CS RENPs and detailed and extensive reviews have been published on that subject.[22-26] Table 1 summarizes the underlying techniques of the principles and processes described in this section for the synthesis of RENPs. The methods for the preparation of the shell depend strongly on the material of both the core and the shell. In principle, it is possible to prepare a shell of the same or different material as the core, although the growth of the shell material on the surface of the core NP will be easier if both materials are identical or have similar lattice parameters, as it will lead to less lattice defects. Very common is the preparation of NPs covered with a shell of amorphous or mesoporous silica, which is very useful not only for protecting the core materials from quenching effects, but also for facilitating subsequent functionalization.[27] In addition, various examples can be found on the combination of RENPs with plasmonic materials as gold or silver, which act as luminescence enhancers or provide plasmonic properties to the NPs.[28] Finally, it is also possible to prepare nanostructures with a combination of different shell materials (sometimes described as core/shell/shell or core/spacer/shell NPs). These structures usually facilitate the growth of materials with very different lattice parameters,

as it is the case of plasmonic materials on fluoride NPs (e.g., $NaYF_4$@SiO_2@Au, $NaGdF_4$:Yb,Er@$NaGdF_4$@Ag, and $NaYF_4$:Yb,Er@$NaYF_4$@SiO_2@Au).[29-32] Additionally, they are used to control the distance between the RE ions and the plasmonic material, which is a fundamental parameter for the enhancement of the luminescence.[28]

Technique	Principle
Thermal decomposition	The precursor materials containing the dopant ions and the matrix components in the desired ratio are mixed in high boiling solvents (usually oleic acid and octadecene) and then heated to elevated temperatures (usually above 280 °C) that induce decomposition of the precursor and crystal formation (nucleation) of the nanoparticles. Precise control of the reaction temperature and time is necessary to achieve homogenous sizes and morphologies.
Solvothermal synthesis	The precursor materials are mixed in a pressure-resistant reaction vessel (autoclave) in the presence of a low boiling solvent that generates pressure in the vessel during the synthesis at temperatures above the boiling point but below the ones used in thermal decompositions. In the case of H_2O the reaction is called hydrothermal and often allows the direct synthesis of water-dispersible NPs although control of size and morphology is less easily achieved.
Microwave-assisted synthesis	This type of synthesis usually combines the above approaches to some extent. The rapid heating of the whole mixture from the inside and the generation of hotspots favour a homogenous thermal decomposition, while the reactions are usually performed in sealed microwave tubes which add pressure as an element that otherwise is the key for solvothermal syntheses.

Table 1. Short summary of the techniques usually employed for the synthesis of RENPs

However, in this review article we focus on the cases where both core and shell contain RE ions. RENPs are usually based on fluorides, oxides, phosphates, vanadates, molybdates, and wolframates as basic inorganic crystals that form the matrix of the NPs. Although the matrix does not have to contain RE ions, these compounds normally facilitate the doping process with other RE ions of interest,[33] hence matrices already including RE ions stoichiometrically are usually employed. Among the mentioned host materials, fluorides are the most commonly used in biological applications.

Fluorides can be prepared following a variety of methods that include thermal decomposition, solvothermal, or microwave synthesis, among others. The preparation of the CS structures is usually a two-step procedure; the synthesis of the core NPs, followed by the addition of the starting material for the shell. This is, for example the case in thermal decompositions, where the strategy followed in Vetrone *et al.* work which represented the first approach for the use of a doped shell to enhance the emission of $NaGdF_4$:Er,Yb UCNPs.[34] The core was prepared by thermal decomposition of RE trifluoroacetates in high boiling organic solvents. After the synthesis of the core NPs was completed, the precursors (also trifluoracetates) of the shell material were injected into the reaction flask, allowing the growth of the new material on the surface of the already formed NPs. In these cases, where the material of the core and the shell are very similar, the formation of the shell is demonstrated by taking an aliquot from the synthesis flask after the first step (core synthesis) and before adding the precursors of the shell in the 2nd step. Then, the comparison of the size of the only core NPs with the ones after the 2nd step should demonstrate an increase in size of the CS NP due to the addition of the shell. The advantage of thermal decomposition methods for the growth of CS NPs is that they make it possible to continue the process in one pot and grow a desired number of shells through the stepwise injection of precursors which form

additional layers or shells on the surface of the NPs without interrupting the synthesis.[35] This layer-by-layer method for the addition of shells has the advantage of providing a very accurate control on the distribution of dopants in the different shells, which reflects in an increase of the luminescence efficiency as demonstrated in the work by Li *et al* (Figure 2a).[36] These authors prepared CS $NaGdF_4$:Yb,Tm@$NaGdF_4$:Ln (Ln = Tb, Eu) NPs that showed an improvement of 20%–30% In their luminescence intensity when compared to the same materials prepared in a one step process.

The disadvantage of the stepwise addition in one pot (layer-by-layer method) is that it usually requires a very precise control of the precursor injections in order to achieve homogeneous growth of the different shells. Therefore, mechanical pumps are often employed for the injection in order to control the temperature of the reaction flask, so it doesn't suffer large variations during the introduction of the colder precursors. This drawback was solved by Quintanilla *et al*.[37] by using a thermal decomposition method based on microwave heating, which allows to reach the synthesis temperature fast enough to achieve homogeneous decomposition of the precursors without dropwise injection and thus, homogeneous formation of the shell. In this case, they prepared small core/shell/shell structures of $NaGdF_4$:Tm,Yb and $NaGdF_4$:Er,Yb NPs. Through the distribution of the dopants in the core and different shells, they modified the intensity ratios of the different emission bands and, therefore, the overall emission colour. Finally, another possibility in thermal decomposition CS synthesis is the use of epitaxial growth for the shell formation, by the injection of small sacrificial NPs as shell precursors in a reaction flask containing the core NPs at 300˚C (Figure 2b-e).[38] The system experiences Ostwald ripening, so the sacrificial particles dissolve and deposit on the surface of the core NPs, forming highly homogenous CS NPs without the requirement of a highly controlled addition of precursors.

Figure 2. (a) (left) Schematic illustration of the dopant distribution when a stepwise addition for the formation of small shells is used (SLBL: successive layer-by-layer) creating a homogenous core (HOC) followed by a final inert shell (S) (right) In contrast, the synthesis of a larger heterogeneous core (HEC) followed by an inert shell (S) results in the concentration of dopants in the center of the core. Reproduced with permission from [36]. Copyright 2014 American Chemical Society. (b-d) TEM of $NaYF_4$:Yb^{3+},Er^{3+} (15/2%) core NPs (b: *t* = 0), after injection of sacrificial α-$NaYF_4$ NCs (c: *t* = 15 s), and after self-focusing $NaYF_4$:Yb^{3+}/Er^{3+} (15/2%) core/$NaYF_4$ shell NCs (d: *t* = 10 min), respectively, and (e) size distribution of the NCs. Reproduced with permission from [38]. Copyright 2012 American Chemical Society.

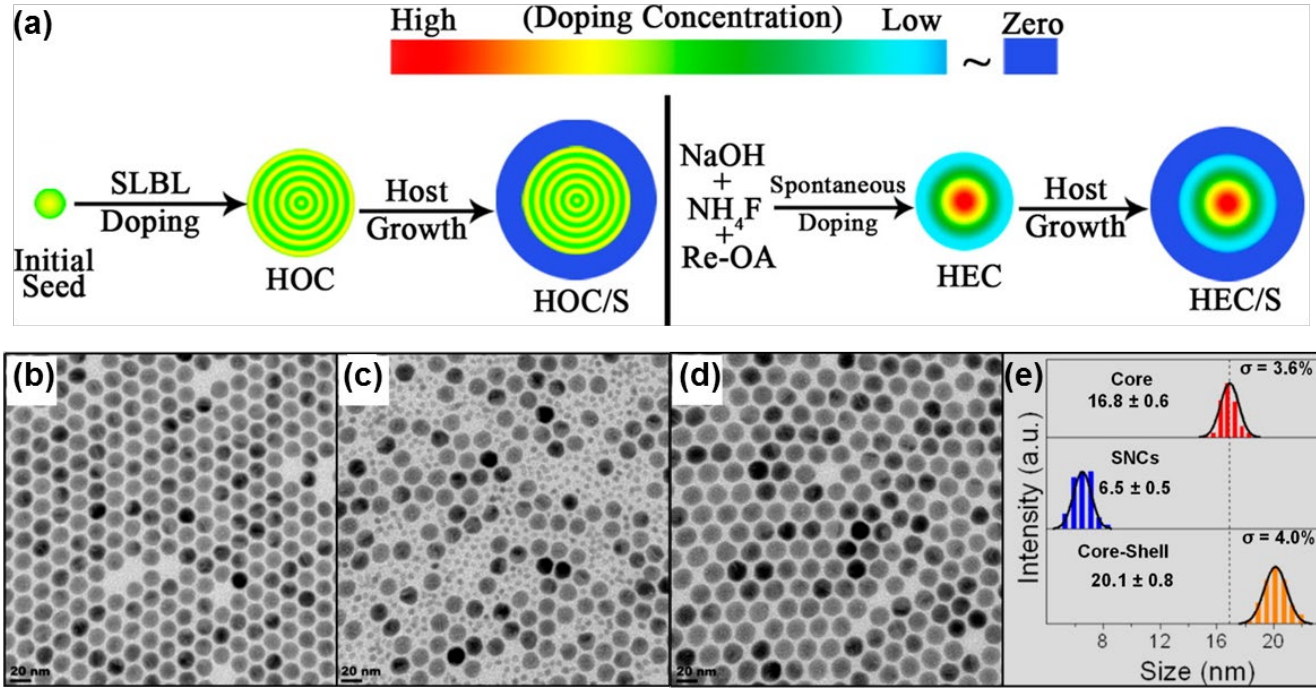

CS nanostructures can also be prepared by solvothermal methods.[39, 40] These procedures usually take longer reaction times and they require the recuperation and washing of the NPs after each synthesis step, so that the precursors for the shell can be added afterwards for the procedure to be repeated. In addition, the shape and size of the NPs is more difficult to control, so that few examples of NPs for biological applications obtained by this route can be found in the literature. However, this approach has the advantage of requiring relatively low temperatures during synthesis, so it is a good method for the preparation of sulfides, oxides, and similar materials, but usually for solid-state applications.[39, 40]

C. RARE-EARTH-DOPED CORE-SHELL NANOPARTILES FOR BIOIMAGING

In this section we highlight the main results achieved in the field of bioimaging by the use of CS RENPs, including results obtained in both *in vitro* and *in vivo* experiments, with special attention to the advantages achieved in respect to previously used optical probes. The section is divided into three sub-sections that aim to reflect the historic evolution of the application of CS RENPs in

the field of bioimaging. In Subsection C.1 it is described how at first CS structures constituted by an inert shell were used to enhance brightness and stability of RENPs and, thus, to improve the quality of bioimages. In Subsection C.2 we review how active core-active shell RENPs have been used to drastically minimize the laser induced thermal loading during *in vivo* imaging experiments just by making it possible to tune the excitation wavelength out of the 980 nm band. Finally, in Subsection C.3 we provide a general overview of the latest advances regarding the use of CS RENPs for multimodal *in vivo* imaging by using the different functionalities of core and shell units.

C.1. Bioimaging with core-shell nanoparticles with an inert shell

The outer shell in CS RENPS, as in other CS structures, usually behaves as isolator, protecting the luminescence of the ions in the inner core from non-radiative de-excitations. They can be produced by surface defects or by the interaction with external emitting units and medium molecules. Indeed, luminescent ions near the NP surface can be directly quenched by passivating ligands, the solvent, surface impurities, and surface lattice defects. Moreover, ions located far from the surface may also suffer from surface quenching effects due to the possible presence of energy migration processes.[41] For instance, widely used Yb^{3+} ions are prone to suffer energy migration processes due to its two-level configuration and long-lived emission. The use of passivating non-doped shells prevents surface quenching as the ions at NP´s surface are not in physical contact with molecules of the medium. This strategy may achieve, in CS RENPs, an increase of the emitted intensity of up to 350 times, enlarging the lifetime more than twice.[42] This enhancement is reflected to a different degree in the intensity of the diverse emission bands of the system.[43-45] The potential brightness enhancement that could be achieved by the use of an inert shell has been demonstrated in different systems. Of special significance are the results provided by Shen *et al.*[46] who studied the enhancement of the emission in UCNPs, comparing the emission of the different crystalline phases of this matrix. α-$NaYF_4$:Yb,Tm@CaF_2 offered triple the intensity in the ultraviolet emission band of Tm^{3+} ions and it was much less quenched than β-$NaYF_4$:Yb,Tm@β-$NaYF_4$ when transferred to aqueous solvents, as shown in Figure 3a. Moreover, these authors observed the rise in the ultraviolet emission in α-$NaYF_4$:Yb,Tm@CaF_2 NPs with the amount of sensitizer ion (Yb^{3+}) in the NP only if the passivating shell was employed (see Figure 3b). This data revealed that the presence of the inert shell does not only provide a way to increase emitted intensities, but also to tailor the spectral properties of the nanostructure. Furthermore, the activation of caged fluorescein in HeLa cells by the enhanced ultraviolet emission of Tm^{3+} ions was studied as an application of the developed CS RENPs (see Figure 3 and Section E of this review for information about photoactivation processes).

At this point we should note that the removal/reduction of non-radiative processes due to the presence of an inert shell was demonstrated to also have a clear signature in the fluorescence decay rates. This was demonstrated by Liang et al.[47] who added a non-doped shell to eliminate vibration-induced non-radiative processes in aqueous dispersions of $NaYF_4$:Nd,Yb@$NaYF_4$:Yb,Tm@$NaYF_4$ NPs (see Figure 4a). The presence of the inert shell lead to a longer lifetime for the $^3H_4 \rightarrow {}^3H_6$

Figure 3. Passivation by CS engineering. Tm^{3+} ions emission intensity in the UV for α-$NaYbF_4$:Tm@CaF_2 and β-$NaYF_4$:YbTm@β-$NaYF_4$ CS RENPs (a) dispersed in hexane and in water (after ligand exchanging; normalized to the Tm^{3+} quantity) and (b) for diverse Yb^{3+} ion (sensitizer) doping in comparison with the emission from core only RENPs (normalized to the total Ln^{3+} concentration; 100 folds for core only RENPs; dispersed in hexane). (c) Confocal microscope scanning of the photoactivation of caged fluorescein in live HeLa cells by the emission of α-$NaYbF_4$:Tm@CaF_2 in the UV under 975 nm laser excitation. Reprinted with permission from [46]. Copyright 2013 Wiley. (d) Schematic illustration of the quenching mechanisms of Er^{3+} emission in the NIR from $NaYF_4$:Er,Yb,Ce@$NaYF_4$ CS RENPs in aqueous dispersion. (e) Quenching rate of Er^{3+} UC and downconversion emission as a function of shell thickness. (f) Er^{3+} emission intensity in the NIR from $NaYF_4$:Er,Yb,Ce@$NaYF_4$ CS RENPs in organic and aqueous dispersion under 980 nm excitation. (g) The blood-flow velocities of cerebral vessels showing the perfusion of the CS RENPs into cerebral vessels (exposure time: 20 ms; scale bar: 2 mm). Reprinted with permission from [50]. http://creativecommons.org/licenses/by/4.0/ Copyright 2017 Nature Publishing Group.

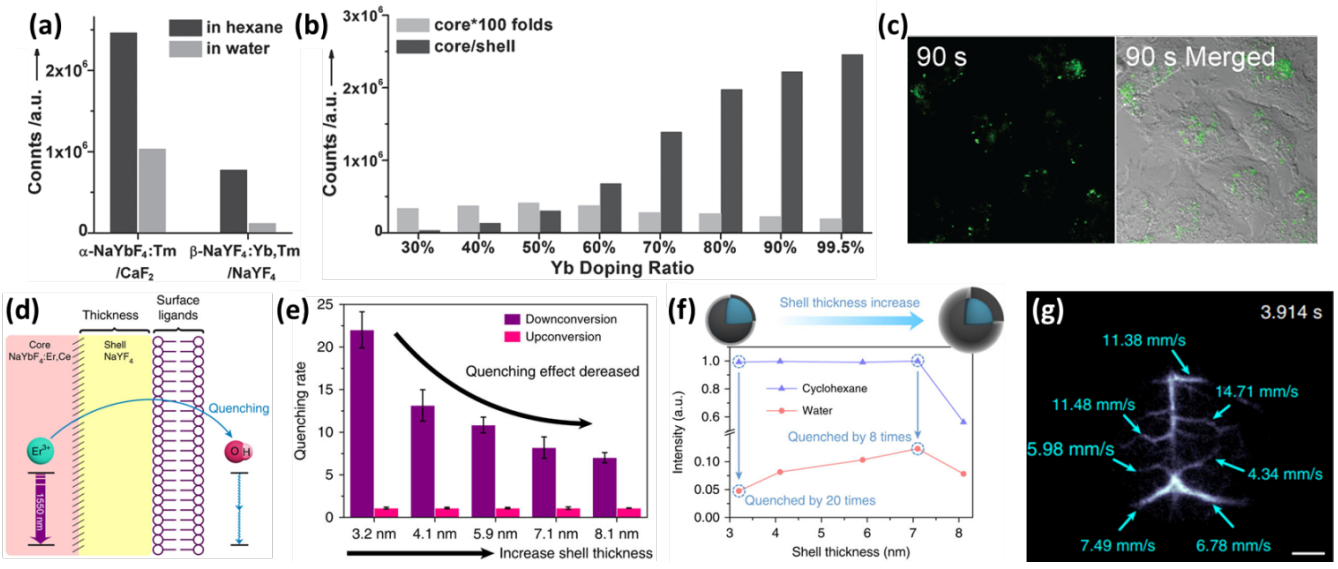

transition of Tm^{3+} ions, as shown in the intensity decay plots of Figure 4c. However, this passivating shell reduced considerably the rate of two-photon population on the $^3H_4$ state of Tm^{3+} ions. Other works have also observed the effect of non-doped shells on the emission intensity of Tm^{3+} ions at about 800 nm, with up to 30 times intensity enhancement and tripled lifetime values.[48]

An interesting question always arises when talking about CS RENPs with inert shells: which is the optimum shell thickness? In this sense, some works have observed that the usual thickness of 1-3 nm is not always fully effective in aqueous dispersions.[49] Zhong *et al.*[50] studied the quenching of the Er^{3+} emission in the third biological window of transparency of the tissues (1500-1800 nm) in $NaYF_4$:Er,Yb,Ce@$NaYF_4$ NPs in aqueous dispersions, which is produced by a two-phonon quenching of the OH^- groups vibrations (see illustrative diagram in Figure 3d). The quenching was assessed depending on the inert shell thickness, as shown in Figure 3e. By increasing the distance between lanthanide ions and surface quenchers, the effect was reduced. For emissions easily quenched by OH^- groups as Er^{3+} in the NIR, an isolating shell of a thickness up to 7 nm is needed to maximize the emission intensity (see Figure 3f). The performance of these NPs was tested in dynamic non-invasive brain vascular imaging with excellent temporal resolution by monitoring the emission of Er^{3+} ions in the third biological window, what allowed the measurement to be performed at high penetration depths in the brain. Figure 3g displays a spatially resolved blood-flow map of the brain, i.e. the plot of the distance travelled by the blood flow as a function of time.

Finally, we should mention that the increase in the brightness of RENPs by surface passivation by CS engineering allowed to reduce the excitation power applied to the specimen and thus the side effects of the procedure.[48] Moreover, in addition to the minimization of interaction between emitting ions and medium molecules, inert shells are being also used to prevent the non-radiative de-excitations produced by outer shells,[51] to avoid energy transfer between active shells with different functions,[43, 52] to impede interparticle ion exchange,[53] and even to include extra functionalities for multimodal bioimaging (see Section C.3.).[52, 54-56]

C.2. Heating-free bioimaging with active core-active shell nanoparticles

The typical sensitization of most VIS emitting RENPs by means of Yb^{3+} leads to an undesired deleterious heating. This is produced due to the overlap of the Yb^{3+} excitation at 975 nm and water absorption at this wavelength, which also shortens the penetration depth of the excitation.[57] Some attempts to excite Yb^{3+} ions avoiding the absorption band of water were made by using different excitation wavelengths, but the low absorption cross section of this ion far from 980 nm makes it impossible to achieve high emission intensities from the activator ions.[45] As a substitute for Yb^{3+} ions, Nd^{3+} has become the preferred sensitizer ion for bioimaging. Its excitation at either 745 or 800 nm, when compared with the typical sensitization by means of Yb^{3+} ions (980 nm), results in better penetration depths and reduced absorption by water molecules. Moreover, the emission lines of Nd^{3+} in the NIR are of great interest as they are within the NIR first and second biological windows (spectral regions within the 700-950 and 1000-1350 nm spectral ranges in which tissues are partially transparent).[58] $Nd^{3+}\rightarrow Yb^{3+}\rightarrow$activator energy transfer has been extensively used over the last years for the development of UC VIS-emitting RENPs without thermal loading and proving an even more intense emission intensity due to the larger absorption cross-section of Nd^{3+} at around 740 and 800 nm.[47, 59] This was possible thanks to CS engineering, as the codoping with Nd^{3+} and activator ions could lead to severe quenching of their emissions so that it becomes essential to separate Nd^{3+} (donors) from VIS-emitting ions (acceptors such as Er^{3+}).[60]

Concerning this challenge, Liang *et al.*[47] studied the heating caused by the excitation at 980 nm and they designed a CS RENP with good prospects for bioapplications under excitation at 745 nm. CS UCNPs were excited at 745 nm, with Nd^{3+} ions as the sensitizer of the Tm^{3+} emission at around 800 nm (see illustrative diagram in Figure 4a). The excitation spectra of this system (see Figure 4b) proved the possibility of exciting Nd^{3+} ions both at around 800 and 745 nm. These excitation wavelengths avoid undesired overheating issues. As shown in Figure 4d, tissue exposed to 980 nm laser irradiation suffered more than 5-fold heating in comparison to when irradiated at 745 nm (under the same experimental conditions). The effect of the overheating produced by a 980 nm laser was also tested *in vitro* with HeLa cells. Cell viability was studied for various irradiation times and, as expected, 745 nm light did not affect cell viability but 980 nm light produced hyperthermia in cells even at low exposure times, as shown in Figure 4e and 4f (see section E for more information about hyperthermia).

Sensitization by means of Nd^{3+} ions presents other advantages. For example, although indirect excitation of Yb^{3+} ions by means of energy transfer from Nd^{3+} may reduce the subsequent UC luminescence intensity, the higher penetration depth of 808 nm excitation results in a more intense signal from the NPs in in vivo experiments, as shown in Figure 4g.[61] In addition, Figure 4h shows the extreme and fast heating of a mouse under irradiation with 980 nm light, while the laser exposure at 808 nm does not produce significant heating even at longer exposure times.[61] This fact is crucial for LNPs-assisted treatments, which usually require long exposure times (see section E).[62]

With a different approach, a tuneable (700-860 nm) and more efficient excitation of LNPs was achieved by Shao *et al.*[63] using indocyanine green organic dye molecules as sensitizers attached to the $NaYF_4$:Yb,X@$NaYbF_4$@$NaYF_4$:Nd (X = null, Er, Ho, Tm, or Pr) NPs surface. The energy absorbed by the dye is transferred to Nd^{3+} ions in the outer shell, which allows to excite Yb^{3+} ions in the inner shell and, by energy migration, to diverse activator ions in the core. This strategy allowed a 4-fold emitted intensity increase in diverse luminescent ions, due to the higher absorption of the dye molecules and the overlap of its emission with the

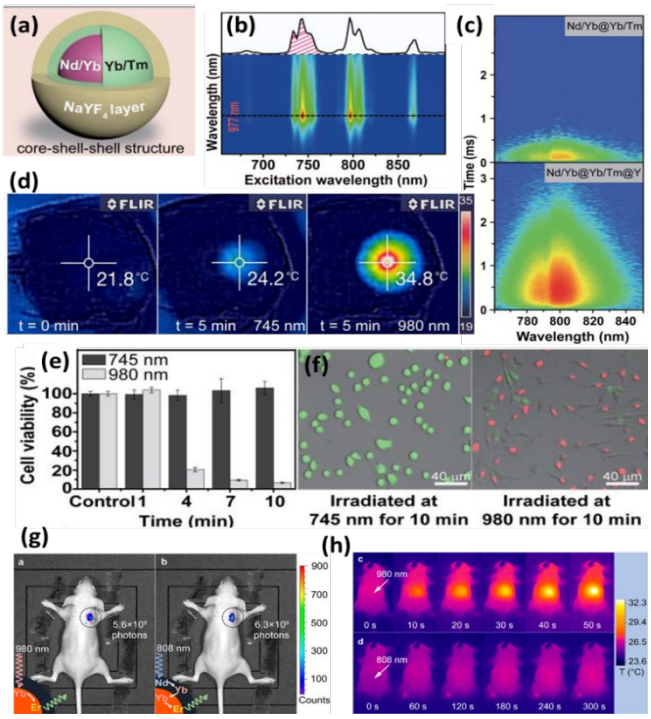

Figure 4. Avoiding deleterious heating due to 980 nm excitation. (a) Schematic illustration of $NaYF_4$:Nd,Yb@$NaYF_4$:Yb,Tm@$NaYF_4$ CS RENPs. (b) Excitation map of these CS RENPs. Excitation spectra at the maximum of Yb^{3+} emission (977 nm) is included on top. (c) Time-resolved emission map of NaYF4:Nd,Yb@NaYF4:Yb,Tm and $NaYF_4$:Nd,Yb@$NaYF_4$:Yb,Tm@$NaYF_4$ CS RENPs under 745 nm excitation. (d) Spatiotemporal temperature distributions on rat back skin before (left) and after irradiation (250 mW cm^{-2} laser power density) for 5 min with 745 nm (centre) and 980 nm laser (right). (e) Cell viability (MTS assays) of HeLa cells irradiated with 745 nm and 980 nm lasers for different time intervals. (f) Fluorescent cellular images after irradiating for 10 min (green and red staining used for labelling live and dead cells, respectively). Reprinted from [47]. Copyright 2016 Wiley-VCH Verlag GmbH & Co. KGaA. (g) *In vivo* UC imaging of a nude mouse subcutaneously injected with $NaGdF_4$:Yb,Er@$NaGdF_4$:Nd,Yb CS RENPs. The images were obtained under 980 nm laser (left) and 808 nm laser (right) irradiation (power density of 200 mW/cm^2; regions of interest are denoted by black dot circles). Insets: schematic diagram of the energy transfer processes under the diverse excitation wavelengths. (h) NIR thermal image of a nude mouse under continuous 980 nm laser irradiation for 50 s (top) and 808 nm laser irradiation for 300 s (bottom). The white arrows denote the irradiation spots. Reprinted with permission from [61]. Copyright 2013 American Chemical Society.

absorption of Nd^{3+} ions. This strategy is crucial for facing the low absorption of lanthanide ions. It has recently been used not only in diverse applications in nanomedicine,[64] but also in renewable energies,[65] for instance.

These advances in CS engineering led not only to thermal loading minimization, but also to a relevant increment of their penetration depth. This was achieved by means of excitation wavelengths that are barely absorbed by tissues, such as 745 and 808 nm.[43, 47] Furthermore, an emission intensity increase due to a more efficient sensitization and the reduction of non-radiative de-excitations can also result in an improved penetration depth.[47, 63]

C.3. Core-shell nanoparticles for multimodal imaging

The chemical similarity but large spectroscopic and physical differences between RE ions make them ideally suited as generators of multifunctionality (or multimodality in the case of bioimaging). This makes it easy to select a range of dopants and embed them in the same NP matrix while generating a wide range of functionalities. This approach is further fine-tuned with the application of CS architectures as discussed in the following paragraphs. Table 2 gives an overview of the application of CS RENPs as contrast agents in combined imaging techniques.

C.3.1. Core-shell nanoparticles for X-ray, computer-based tomography, and magnetic resonance imaging

The most commonly applied imaging techniques in the clinic are radiography and computer-based tomography (CT), both based on X-rays. They are routine techniques in whole body as well as organ imaging. Therefore, multimodal NPs that not only present the potential for optical bioimaging, but also can act as CT contrast agents have a high potential to advance RENPs into commercial applications. Here NPs with a high amount of heavy lanthanides can work as X-ray attenuators and thereby enhance the contrast.

The first CS RENPs capable of CT contrast were presented in 2013 based on a $NaLuF_4$ core,[66] being Lu the heaviest of the RE ions, and a protecting $NaGdF_4$ shell (also useful for magnetic resonance imaging (MRI) thanks to Gd ions). Furthermore, the 4 nm thick $NaGdF_4$ shell was doped with traces of radioactive ^{153}Sm as a single photon emission computed tomography (SPECT) contrast agent. This structure, schematically depicted in Figure 5e, allowed for combined optical, CT, MRI, and SPECT imaging, as shown in Figure 5a-d and 4f.

During the same year, Shen *et al.*[67] presented a four-layer multimodal $NaYF_4$-based design with two inner shells, one of them containing $NaLuF_4$ for CT imaging and a second inert $NaYF_4$ shell, combined with the first one, used for separating the UC $NaYF_4$:Yb,Tm core from the thin outer $NaGdF_4$ layer aimed for MRI. This separation was necessary in order to prevent quenching of the activator Tm^{3+} ion in the core, responsible for optical imaging, via Tm→Gd energy transfer. This demonstrates how a rational design of the employed shells can help with multifunctionality.

Later in 2014, Wang *et al*.[55] presented a multi-shell (2 active, 1 inert) approach for multimodal UC bioimaging. Sensitizer Nd^{3+} ions were placed in the next-to-outer-shell, from which energy transfer to the Er^{3+} doped core took place via Yb^{3+} ions in the inner shells and the core. The core and the shells were based on $NaLuF_4$ as matrix, presenting excellent contrast properties in CT scans in both *in vitro* and *in vivo*, while the core also contained Gd^{3+} ions improving the T1-relaxivity and adding MRI-imaging to the multimodal capabilities.

Table 2. Core-shell nanoparticles used for multimodal imaging in the different discussed examples. The imaging techniques which are combined with inherent luminescence are detailed.

CS RENP	Additional imaging techniques			Reference
	CT / X-ray	MRI	Others	
$NaGdF_4$:Yb,Er@$NaGdF_4$	X	X		44
$Na_{0.52}YbF_{3.52}$@SrF_2	X	X		45
$NaYF_4$:Yb,Er@$NaGdF_4$@SiO_2		X		54
$NaLuF_4$:Gd,Yb,Er@$NaLuF_4$:Yb@$NaLuF_4$:Nd,Yb@$NaLuF_4$	X	X		55
$NaYF_4$:Yb,Er,Tm@$NaGdF_4$@TaO	X	X		56
$NaGdF_4$:Yb,Er@$NaGdF_4$:Yb@$NaGdF_4$:Yb,Nd@$mSiO_2$		X		59
$NaGdF_4$:Yb,Er@$NaGdF_4$:Nd,Yb		X		62
$NaLuF_4$:Yb,Tm@$NaGdF_4$(^{153}Sm)	X	X	SPECT	66
$NaYF_4$:Yb,Tm@$NaLuF_4$@$NaYF_4$@$NaGdF_4$	X	X		67
$NaYF_4$:Yb,Er@$NaGdF_4$:Yb@$mSiO_2$+ZnO	X	X		68
$Y(OH)CO_3$:Yb,Er@$Y(OH)CO_3$:Yb	X			69
$NaGdF_4$:Yb,Er@$NaGdF_4$:Yb@$mSiO_2$-Dopa	X	X		70
$NaGdF_4$:Yb,Er@$NaGdF_4$		X		71
$NaYF_4$:Yb,Tm,Gd@$NaGdF_4$		X		72
$NaDyF_4$:Yb@$NaLuF_4$:Yb,Er@polydopamine		X		73
$NaGdF_4$:Yb,Er@$NaGdF_4$:Yb@$NaNdF_4$:Yb+Au_{25}			PA	74
$NaGdF_4$:Nd@$NaGdF_4$:Yb,Er@$NaGdF_4$:Yb@$NaNdF_4$:Yb+Au_{25}			PA	75
$NaYbF_4$:Tm@$NaYF_4$@porphyrin-phospholipid	X	X	PA, PET, Cherenkov	76
$NaYF_4$:Yb,Er@Yb,Nd@SiO_2+ICG			PA	77

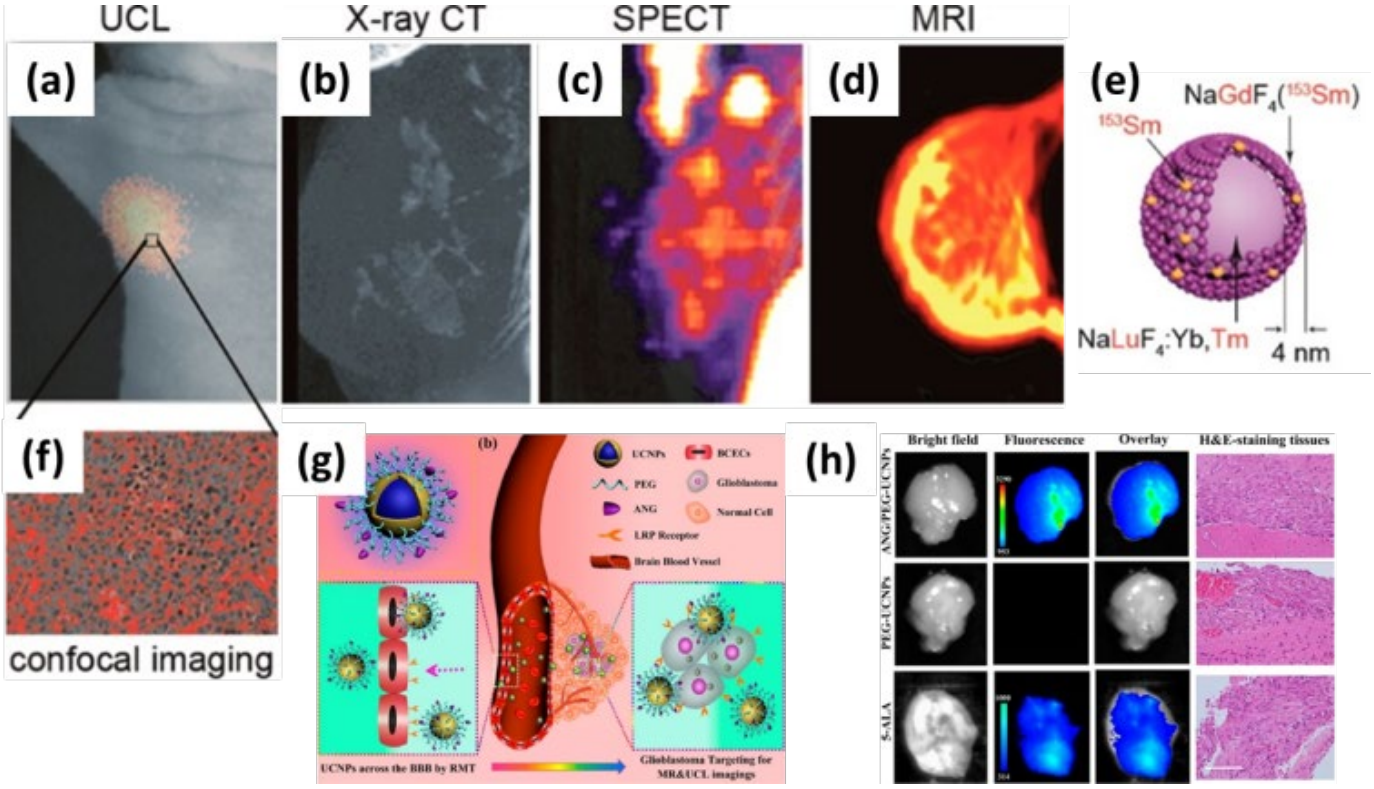

Figure 5. CS RENPs for multimodal imaging. *In vivo* (a) UC luminescence (ex. 980 nm), (b) CT,)c) SPECT, and (d) MRI Images (false colours) of UC CS RENP-marked tumour on mouse 1 h after intra venous injection. (e) Schematic representation of the $NaLuF_4$:Yb,Tm@$NaGdF_4$ (^{153}Sm) UC CS RENPs employed in a-d and f. (f) Confocal UC luminescence microscopy of an *ex vivo* paraffin section of the tumor demonstrating the presence of UCNPs inside the tissue. Reprinted with permission from [66]. Copyright 2013 American Chemical Society. (g) Another example of the use of UC CS RENPs for bioimaging. Schematic representation of the experiment where CS RENPs were functionalized with a protein (ANG) to recognize angiogenesis of glioblastomas and thereby pass the blood-brain barrier. (h) *Ex vivo* brightfield and luminescence images of mice brain 1 h after injection. The top row shows ANG-functionalized UCNPs that have passed to the brain and mark the tumour region with a strong signal. Unfunctionalized UC CS RENPs in middle row do not target the area of interest. Bottom row shows a control experiment where a dye passes through blood-brain barrier but it does not selectively mark the tumour. The right column shows stained histograms demonstrating the presence of glioblastoma. Reprinted with permission from [72]. Copyright 2014 American Chemical Society.

In 2014 Tian *et al*.[44] demonstrated that $NaGdF_4$:Yb,Er UC RENPs coated with an inert shell of the same matrix were not just capable of UC optical imaging and acting as MRI contrast agents, but also respectable radio attenuators. The presence of heavy Gd and Yb was sufficient to achieve better CT contrast than with commercial contrast agents, thus no integration of Lu in the structure was necessary.

One of the earliest examples of CS NPs with radio attenuation in the literature dates from 2012.[56] Typical RENPs for UC luminescence imaging ($NaYF_4$:Yb,Er,Tm) were converted into multimodal imaging agents by adding a $NaGdF_4$ shell and decorating it with a heterogeneous TaO_x layer. The TaO_x layer had the form of small NPs in silica with added PEG for better water dispersibility and resulted in 30 nm sized NPs with a rough/dented surface due to the TaO_x NPs decorating the surface. Ta presented, together with the Gd, an excellent CT and MRI contrast without impeding the UC luminescence. This multimodal ability was demonstrated in trimodal imaging experiments in mice.

In 2016 the Lin's group presented an interesting approach to improve the optical imaging of trimodal (UC luminescence, CT, MRI) $Na_{0.52}YbF_{3.52}$@SrF_2 CS RENPs.[45] The scarcity of Na during the synthesis created sub-stoichiometric particles with an improved red emission facilitating the UC luminescence imaging, while CT and MRI contrast were achieved solely based on Yb^{3+} ions.

Wang *et al*.[68] presented in 2015 UC RENPs for trimodal imaging with an added mesoporous silica-shell for drug delivery, which also allowed them to vary the CS architecture by placing Yb^{3+} not just in the $NaYF_4$:Yb,Er core, but also in the intermediary $NaGdF_4$:Yb shell, while the outermost shell was mesoporous silica decorated with ZnO quantum dots as gatekeepers for drug release in an acidic medium. A similar approach was previously reported employing Tm^{3+} instead of Er^{3+} and a different surface functionalization. This example is discussed in Section E.1.

The only non-fluoride CS host also employed for multimodal bioimaging was reported by Lv *et al.* in 2015.[69] Their CS RENPs were designed mainly for drug delivery and therapy (for more details see Section E), but they are an interesting example of oxide-based

CS structure, which was obtained in a controlled calcination of the hydroxyl carbonates of the lanthanides $Y(OH)CO_3$:Yb,Er@$Y(OH)CO_3$:Yb. As can be seen from the dopants, these CS RENPs allowed UC luminescence bioimaging and provided CT contrast, which was demonstrated in mice. Recently Lv et al.[70] also reported multifunctional and multimodal UC CS RENPs based on a more typical architecture ($NaGdF_4$:Yb,Er@$NaGdF_4$:Yb@$mSiO_2$-Dopa), thereby achieving smaller particle size and adding MRI to the imaging capabilities.

One of the first CS based multimodal imaging (MRI and luminescence) examples had already been published in 2009 by Park *et al*.[71] They studied functionalized $NaGdF_4$:Yb,Er@$NaGdF_4$ NPs in cellular models and were able to perform single particle luminescence imaging with a modified atomic force microscopy setup, demonstrating the brightness increase achieved by incorporating the shell.

Ni *et al*.[72] presented UC CS RENPS with an inert $NaGdF_4$ shell ($NaYF_4$:Yb,Tm,Gd@$NaGdF_4$) and functionalized with PEG and a short peptide for Glioblastoma targeting (Angiopep-2) that were employed to image brain tumours with MRI *in vivo* and with UC luminescence *ex vivo*. Figure 5g schematically shows the particle design and the targeting process of the glioblastoma by means of the peptide. Figure 5h demonstrates the precision of the targeting by fluorescence imaging of the excised brain and a comparison with classical staining of the tissue sample.

A multifunctional dual imaging probe (MRI and UC luminescence) with a rational design for excitation at 808 nm, was presented by Li *et al*.[62] in 2016 with a CS architecture ($NaGdF_4$:Yb,Er@$NaGdF_4$:Nd,Yb) placing Nd^{3+} ions as sensitizer in the shell and employing Yb^{3+} for energy transfer to the core, in order to achieve Er^{3+}-based UC luminescence, but also employing the Yb^{3+} emission at 980 for NIR imaging. This allowed the combination of optical imaging with T2-weighted MRI based on Gd, while also adding a sensitized-dye for photodynamic therapy (PDT, see section E.2) excited by UC luminescence.

Zeng *et al*.[59] also presented 808 nm excited CS RENPs for a theranostic approach against breast-cancer. They presented functionalized and silica-coated core-shell-shell NPs ($NaGdF_4$:Yb,Er@$NaGdF_4$:Yb@$NaGdF_4$:Yb,Nd@$mSiO_2$), whose UC luminescence was employed in in mice models and the Gd of the host matrix for MRI. The intermediary $NaGdF_4$:Yb shell was included to achieve a larger separation between the sensitizing Nd^{3+}ions and the emitting Er^{3+} ions in the core. In this manner, energy back transfer from the activator to the sensitizer was suppressed. The mesoporous silica shell included covalently attached Ce6, an organic dye for PDT, which was activated through the UC luminescence. Furthermore, functionalization of the surface with a peptide helped with active targeting of the Her2 breast cancer.

Fan *et al*.[54] presented already in 2013 a hollow shell approach for theranostic application in cancer treatment. They synthesized a typical CS structure for multimodal imaging (UC luminescence and MRI) $NaYF_4$:Yb,Er@$NaGdF_4$, on which they added two layers of dense silica and finally PVP as a surface coating. This allowed them to treat the silica layers away from the inner layer with hot water etching while the outer layer was mostly protected by the polymer and therefore only slightly attacked, converting itself into a mesoporous silica shell around a cavity that included the UC CS RENPs. In this manner a so called rattle or yolk shell (YS) structure was obtained that was additionally loaded with cis platin for chemo- and radiotherapy. The YS RENPs were successfully employed in murine studies for the treatment of HeLa tumours.

Dual-mode MRI-imaging (T1 and T2) and UC luminescence via a CS architecture was presented in 2016 by Zhou's group.[73] Preferring the also paramagnetic Dy over typically employed Gd, they synthesized CS $NaDyF_4$:Yb@$NaLuF_4$:Yb,Er@polydopamine, achieving water-dispersibility and biocompatibility through surface-coating with polydopamine. Furthermore, they modified the polydopamine with EDTA and complexed Mn^{2+} on the CS RENPs. They demonstrated *in vivo* T2-weighted-imaging based on Dy and T1-weighted-imaging based on the Mn-complex on the surface. Additionally they were able to show the potential for photothermal therapy (see section E.3) due to heating by the polydopamine when excited at 980 nm.

C.3.2. Core-shell nanoparticles for photoacoustic imaging

In recent years, photoacoustic (PA) imaging has become a popular technique combining the PA effect (absorbed energy generates heat and a thermoeleastic expansion which causes a wideband ultrasonic emission) with ultrasound techniques. Usually, intrinsic chromophores as haemoglobin or organic dyes that absorb pulsed laser radiation are employed and the ultrasonic signal is received by transducers and analysed. UC CS RENPs therefore can also be modified with strongly absorbing PA agents for a different form of multimodal imaging.

In 2015 He *et al*.[74] combined $NaGdF_4$:Yb,Er@$NaGdF_4$:Yb@$NaNdF_4$:Yb CS RENPs excitable at 808 and 980 nm with Au_{25} nanoclusters. These CS RENPs were loaded into a mesoporous silica shell and further functionalized with a PEG-surface coating. Not only the gold nanoclusters were able to perform PDT, but their strong absorption and heating capabilities also resulted in the addition of a PA imaging modality to the UC luminescence of the UC CS RENPs. In 2016 they expanded on this work by changing the core and the inner layer presenting $NaGdF_4$:Nd@$NaGdF_4$:Yb,Er@$NaGdF_4$:Yb@$NaNdF_4$:Yb as CS RENPs with better heating and imaging capabilities and then adding the gold nanoclusters. As was the case in the first example, they demonstrated photoacoustic imaging *in vivo*.[75]

Demonstrating the possible versatility in bioimaging by means of UC CS RENPs, Rieffel *et al.*[76] added PA imaging via surface functionalization with a porphyrin-phospholipid to $NaYbF_4$:Tm@$NaYF_4$ UC CS RENPs. This also allowed the easy labeling of porphyrine with radioactive ^{64}Cu, also allowing for positron emission tomography (PET) and Cherenkov multimodal imaging. This was achieved in addition to the luminescence (UC and porphyrine-based) and CT-contrast already provided by the core and inert shell of the NP. Rieffel *et al.* successfully used this multimodal nanoplatform to visualize the lymphatic node in a hind leg of mice.

In 2017 Prasad's group[77] presented 808 nm-excitable UC CS RENPs that had an additional mesoporous silica shell loaded with an NIR organic dye and it was sealed through treatment with TEOS, preventing the release of the dye (Indocyanine green). This allowed them to present *in vivo* dual mode imaging in the form of UC luminescence and PA imaging with the FDA-approved dye. Storing the dye inside the silica layer helped to protect it from the biological environment and to transport it to the desired location. Additionally, the group demonstrated that the CS RENPs were also good nanoheaters and that their nanomaterial could be also employed in photothermal therapy.

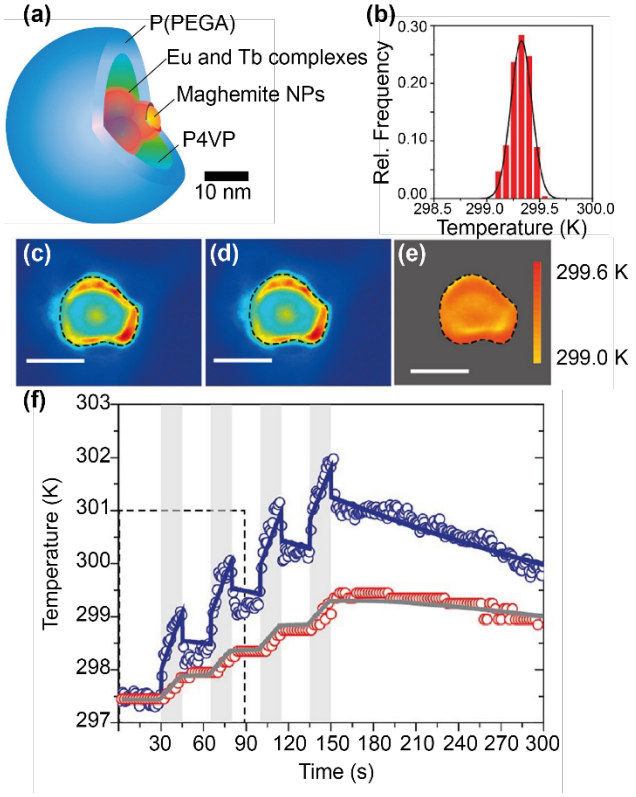

Figure 6. (a) Schematic scaled representation of an optical-magnetical NP. In the central region, Eu^{3+} and Tb^{3+} complexes (reddish layer) for temperature measurement cover the maghemite NPs (orange). The P4VP (green) forms a first shell encapsulating the magnetic NPs and the P(PMEGA-*co*-PEGA) chains (blue) occupy the outer part. (b) The histogram of the temperature distribution near the opossum kidney cells´ nucleus and its fit to a Gaussian distribution of mean value 299.3 ± 0.2 K, in agreement with the cell culture temperature. Temperature mapping of OK cells, showing the (c) Eu^{3+} (around 610 nm) and (d) Tb^{3+} (around 545 nm) emissions. The interrupted lines delimitate the nucleus of the opossum kidney cell, marking the region of interest within which the temperature map showed in (e) was computed. All scale bars correspond to 10 µm. (f) Temperature measurement of the same suspension during a 300 s multipulse experiment using the molecular (blue circles) and semiconductor (red circles) thermometers. The shadowed areas mark the time intervals when the magnetic field is turned on (15 s). The solid lines correspond to the fit of experimental data with the lumped elements model. Adapted with permission from [78]. Copyright 2015 American Chemical Society.

D. CORE-SHELL RARE-EARTH-DOPED NANOPARTICLES FOR BIOSENSING

In this section a general view of the latest advances achieved in the field of biosensing by using CS RENPs is provided. Biosensing is here defined in a wide sense. We consider that biosensing is being achieved when additional information, different from biodistribution, is obtained from the analysis of the bioimages produced by using the CS RENPs. When revisiting the literature, the CS RENPs employed for biosensing can be classified into two main blocks: thermal and molecular/chemical biosensing. Accordingly, this section is structured into two subsections. Section D.1 aims to provide the reader with a general description of the state of the art regarding the use of CS structures for thermal sensing in biological systems. Then, Section D.2 provides some examples in which CS RENPs have been used for chemical biosensing.

D.1. Core-shell rare-earth-doped nanoparticles for thermal sensing

The most frequent application of RENPs for sensing is in thermometry, due to the sometimes outstanding thermal sensitivity of RE ions. The synergy between nanothermometry, CS engineering, and nanomedicine led to the appearance of self-referenced heating agents for thermal therapies. The first example was the work published by Piñol *et al.*[78] in 2015, demonstrating how a CS structure was able to provide real time thermal control to magnetic nanoparticles (see Figure 6a). The thermometer/heater NP was an iron oxide surrounded by Eu^{3+} and Tb^{3+} complexes and overall coated with a copolymer (P4VP-*b*-P(PMEGA-*co*-PEGA)), as shown in Figure 6a. In this structure the core was the magnetic heater, while the shell was a thermosensitive luminescent unit. The authors developed this CS structure to improve the efficacy of the localized magnetic heating and to obtain optical temperature readout. Temperature sensing was obtained by means of the UV excited Tb^{3+} and Eu^{3+} emission bands centred at 545 and 615 nm, respectively. The ability of this RE doped coating for accurate thermal sensing was demonstrated by performing simple *in vitro* experiments by analysing fluorescence cellular images after incubation with CS NPs as those represented in Figure 6(a). Figure 6c and 6d shows, respectively, the fluorescence images corresponding to a single kidney cell as obtained by detecting the emission intensities at around 540 nm (Tb^{3+}) and 610 nm (Eu^{3+}). The thermometric mapping at subcellular scale (Figure 6e) was obtained by simply taking the ratio of the images in Figure 6c and 6d. Piñol *et al.* claimed a temperature resolution as good as 0.5 K from the

temperature histogram included in Figure 6b. The good thermal sensitivity of the luminescent shell was then applied to real time monitoring of the local heating produced when an alternating magnetic field was applied to a colloidal suspension of these optomagnetic CS structures (see Figure 6f). The demonstration of simultaneous magnetic heating and thermal sensing provided by Piñol *et al*. had a great practical impact, since it does not only show the possibility of thermal control in magnetic thermal therapies, but also opened the door to the study of thermal dynamics at the nanoscale.

A successful example of thermal sensing achieved in living animals by means of CS RENPs was provided by LaF_3:Nd@LaF_3:Yb CS NPs. [79] These NPs are constituted by a Nd^{3+} doped core and a Yb^{3+} doped shell. When optically excited at 790 nm, energy transfer from Nd^{3+} to Yb^{3+} ions can occur, assisted by energy migration between Nd^{3+} ions. As a consequence of energy transfer processes, radiative decays from the metastable states of both Nd^{3+} and Yb^{3+} ions take place simultaneously, resulting in a multi-band emission in the second biological window. Due to the spatial separation between Nd^{3+} and Yb^{3+} ions, the spectral distribution of the overall emission spectrum results strongly temperature dependent. The NIR thermal sensitivity provided by the ratiometric analysis of the luminescence generated by LaF_3:Nd@LaF_3:Yb NPs was close to 0.4% $°C^{-1}$, which is good enough to achieve subdegree thermal readings. In fact, the CS RENPs ability for accurate measurement of *in vivo* subcutaneous thermal transients (see scheme of the experiment in Figure 7a) is a potential theranostic tool successfully explored by Ximendes *et al*.[79] The physical principle behind the experiment relied on the fact that when a tissue undergoes a thermal relaxation (temperature decrease in the absence of any heating source, see Figure 7a and 7b), the cooling dynamics strongly depends on the intrinsic properties of the tissue. Thus, an accurate measurement of the cooling relaxation profile is capable of providing information on the tissue status and could be used to detect anomalies caused by incipient diseases such as dehydration, inflammation, tumour growth, or even ischemia, as recently demonstrated.[80] Indeed, the analysis of the thermal relaxation curve of a tissue (included in Figure 7b) provides, simultaneously, accurate and consistent values for the tissue thermal conductivity and absorption. This work supported the validity of the use of CS RENPs as accurate and reliable subcutaneous thermal sensors for *in vivo* applications.[81-84]

In the past few years, various CS RENPs emitting in the second biological window while being excited by a wavelength within first biological window have been reported as promising nanothermometers. Recently, Skripka *et al.*[85] presented an optical nanothermometer working within the third biological window. It consisted in a multishell system of β-$NaGdF_4$ with the core doped with Er^{3+}, Ho^{3+}, and Yb^{3+}, a first shell doped with Yb^{3+}, a second shell doped with Nd^{3+} and Yb^{3+} and an undoped passivating outer shell. The temperature dependent energy transfer between the Ho^{3+} - Nd^{3+} and Er^{3+} - Nd^{3+} NIR emission bands pairs presented a maximal thermal sensitivity in the physiological temperature range of 1.17 ± 0.04 % $°C^{-1}$. This system constituted the very first nanothermometer working in aqueous environments within the second (Ho^{3+}/Nd^{3+}) and third (Er^{3+}/Nd^{3+}) biological windows.

Despite of these proofs of the ability of CS RENPs for local thermal reading, many challenges remained to be faced in the field of luminescence if it is aimed to apply it at the pre-clinical level. For instance, the acquisition of two-dimensional subcutaneous thermal images (2D-SDTI) is nowadays required for thermal-based diagnosis. This challenge has been recently overcome by using LaF_3:Er,Yb@LaF_3:Tm,Yb CS RENPs.[86] The temperature dependent non-radiative energy transfer between Tm^{3+} and Yb^{3+} ions results

Figure 7. Temperature sensing with CS RENPs. (a) Schematic representation of the subcutaneous thermal relaxation experiments. (b) Time evolution of the temperatures measured by the subcutaneous luminescent thermometer (grey) and by the IR thermal camera (yellow). Dots are experimental subcutaneous (circles) and skin (squares) temperatures, whereas the solid line is the best fit. Adapted with permission from [79]. Copyright 2016, American Chemical Society. (c) Schematic representation of the *in vivo* 2D-SDTI experiment. Thermal images obtained by dividing the luminescence images at 1000 and 1200 nm during heating (d) and relaxation (e) processes. An optical figure of the anesthetized mouse was superimposed. (f) Time evolution of the average temperature of the injection area as measured by the subcutaneous LNThs during heating and thermal relaxation processes. Reproduced with permission from [86]. Copyright 2017, Wiley.

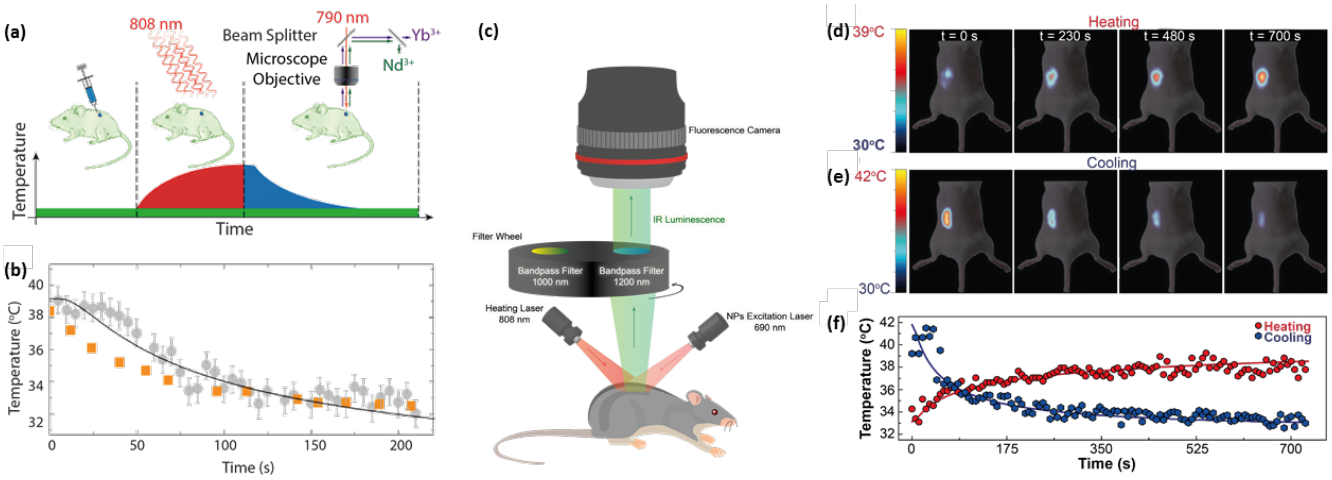

in a multiband emission spectrum within the second biological window. Ratiometric thermal sensitivities as large as 4% $°C^{-1}$ were achieved when monitoring the intensity ratio between the emitted intensity of Yb^{3+} ions at 1000 nm and that of Tm^{3+} ions at around 1230 nm. This superior thermal sensitivity together with their emissions in the second and third biological windows made the achievement of *in vivo* time resolved 2D-SDTI possible. The simple experimental set-up required for 2D-SDTI is schematically shown in Figure 7c. Figure 7d and 7e includes the ratiometric thermal *in vivo* images obtained at different times during heating and cooling processes. The time evolution of the subtissue temperature (see Figure 7f) allowed the estimation of the thermal diffusivity of living tissue.[87] The thermal diffusivity of living tissue provided by CS NPs was found to be in excellent agreement with those reported in the literature. Such agreement supports the validity of using CS RENPs as accurate and reliable probes for diagnostic procedures based on the acquisition of 2D-SDTI.[79] Indeed, the results obtained by Ximendes *et al*. opened the venue to new diagnosis and control techniques that could revolutionize existing methods in biomedicine.

D.2. Core-shell rare-earth-doped nanoparticles for biological labeling

RENPs can also be suitably conjugated with appropriate molecules as effective probes for biological labeling and biosensing.[88] For a description of the recent development of the RE-based luminescence biolabelling, we recommend the review by Sy *et al*.[89] The use of the CS engineering as method of improving the biological labelling, however, is something still in development, although the advantages of using these structures, reported in previous sections, will foster the advance of this field.

The detection of single nucleotide polymorphisms (SNPs) is very important for the diagnosis of various diseases. The existing methods for the detection of SNPs, however, are based on quantitative RT-PCR (reverse transcription polymerase chain reaction), which is a time-consuming and expensive method. Fortunately, CS engineering provides an alternative method. CS RENPs are used for labelling DNA fragments. Fe_3O_4/Gd_2O_3:Eu magnetic and luminescent CS NPs were functionalized with neutravidin and then coupled to probe DNA fragments (complementary of the target DNA carrying a polycystic kidney disease mutation).[90] Genomic DNA was then extracted from the tissue and the region of study (the one containing the polymorphism) was amplified and hybridized with a complementary strand labelled by an organic dye. When the sample DNA and the probe DNA coupled to the CS NP are mixed, hybridization takes place preferentially for the correct SNP. The hybridized fragments containing CS NPs are separated from the solution by a magnet and the luminescence ratio between Eu^{3+} and organic dye reveals the fraction of bound DNA. The presence of a given polymorphism is thus detected by means of the luminescence. The combination of quantification by luminescence and magnetism for separation yields a powerful method for quantitative detection of SNPs.

Another representative example of biosensing by CS RENPs can be found in the pioneering work published by Zou *et al*.,[91] who designed and synthesized a ClO^- detection system based on a Nd^{3+}-sensitized UC CS RENP. As represented in Figure 8a, the authors developed a complex nanosystem whereby a core, constituted by a $NaYF_4$:Yb,Nd,Er NP, was surrounded by an active shell of $NaYF_4$:Nd that would act as an energy donor and

Figure 8. Biological labeling with CS RENPs. (a) Schematic illustration of a CS nanosystem able to sense the presence of ClO^- molecules by a change in its UC emission. When ClO^- is added, the structure of hCy3 changes, resulting in a decrease in its absorption that leads to an increase in the green UC emission. (b) UC luminescence spectra of the CS RENPs under 808 nm excitation in aqueous solution upon gradual addition of NaClO (from 0 to 80 μM). Inset shows the ratio of the UC luminescence emission at 540 nm to 654 nm as a function of NaClO concentration. Ratiometric upconversion bioimages in living HeLa cells (top, c-g). Emission was collected by a green UC luminescence channel at 500–560 nm (d and i) and a red channel at 600–700 nm (e and j). (f and k) Overlay of green UC luminescence and red upconversion bioimages. (g and l) Ratiometric UC bioimages (ratio of green to red channels). In vivo UC luminescence images of the arthritis living mouse with injection of 50 μL complex nanosystem in the left leg and right leg ankles under an excitation power density of 400 mW cm^{-2} (λex = 808 nm, λUCL = 530 ± 25 nm). Reproduced with permission from [91]. Copyright 2015, Royal Society of Chemistry.

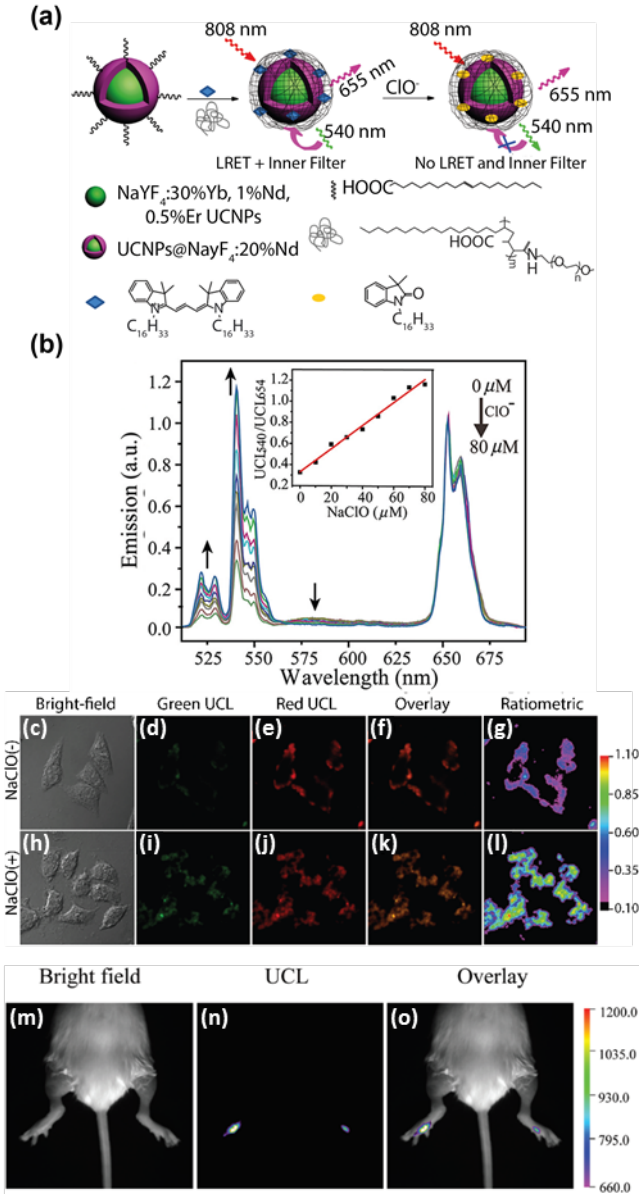

a ClO^- responsive cyanine dye hCy3 as an energy acceptor. When such nanostructures were excited using a 808 nm laser, the Nd^{3+} ions acted as sensitizers to produce UC emissions from Er^{3+} (see Figure 8b) by energy transfer through Yb^{3+} ions. It should be highlighted that the UC emission of $NaYF_4$:Yb,Nd,Er@$NaYF_4$:Nd CS RENPs was significantly enhanced when compared to the simple $NaYF_4$:Yb,Nd,Er RENPs. Furthermore, as the broad absorption band of hCy3 (450–580 nm) matched with the green UC emissions of Er^{3+}, these bands were modulated by the presence of ClO^-, which arose from the reaction between hCy3 and NaClO. The ClO^- could react with the conjugated cyanine dyes (to form the corresponding oxindole), reducing its ability to absorb the green emission bands from UC CS RENP, thus green emission increases as the ClO^- concentration does. In addition, due to the small overlap between the 630-670 nm red emission band of the CS UC RENPs and the absorption band of hCy3, the red UC emission was not influenced by the presence of ClO^-, thus it was used as a reference parameter (see Figure 8b). Inset in Figure 8b shows the change in the intensity ration between green and red emission bands as a function of NaClO concentration, which evidences an increase in ClO^- concentration. The real potential of these complex nanostructures for the detection of small variations on ClO^- concentration was successfully demonstrated in *in vitro* and *in vivo* experiments. In the case of *in vitro* experiments the presence of ClO^- was detected by ratiometric UC luminescence imaging under 808 nm excitation (see Figure 8c-l). In the absence of ClO^-, an initial luminescence imaging investigation revealed low signal intensity for green emission band and a relatively intense red emission band (figure 8d and 7e). However, after the consecutive incubations with 5μM NaClO for 30 min and the complex nanosystems, a great enhancement in the green emission band was observed in the intracellular region, showing an increase in ClO^- intracellular concentration. This result show the potential of the use of ratiometric upconversion luminescence imaging between 500–560 nm and 600–700 nm emission bands as the detection signal, as shown in Figure 8g, with an emission ratio of < 0.4. This result was further improved when the authors used NaClO pre-treated HeLa cells. They were able to increase the ratio up to 0.85 (Figure 8l). This nanosystem was also used to detect ClO^- in an in vivo model of arthritis. This result is illustrated in Figure 8m-o that shows the spatial distribution of the mission ratio generated by UC nanoparticles injected into the two limbs. Note that the left limb, subjected to an arthritis artificial induction, displayed a larger emission ratio than the health (control) right limb.

Finally, we must emphasize that CS engineering is being used nowadays in many different ways to develop advanced biological labelling techniques. For instance, Chen *et al*.[92] have reported CS RENPs capable of highly-sensitive multiplexed biomolecule detection by Z-contrast imaging. They have designed an encoding system based on different structures of UC CS RENPs, which present different contrast in each shell depending on the atomic number of the RE doped in that shell when viewed under scanning transmission electron microscopy. For this reason, we must expect a great deal of interest in the use of CS RENPs for biological labelling applying diverse techniques.

E. CORE-SHELL RARE-EARTH-DOPED NANOPARTICLES FOR THERAPY

In previous sections the application of CS RENPs for advanced bioimaging and biosensing has been described in detail. The breakthroughs achieved in these fields can be considered as advances in the diagnosis, as the information provided by CS RENPs can be used to detect, in early stages, diseases and biological malfunctions. In this fifth section we go further and provide a general review of the latest experimental works demonstrating the potential use of CS RENPs as therapeutic agents. In subsection E.1 we describe how CS RENPs have been used as triggering units for therapies based on fully controlled drug delivery. Subsection E.2 describes how CS RENPs can be used to develop photoactivation therapies. Finally, in strong relation with subsection D.1, subsection E.3 is devoted to provide a general review of the use of CS RENPs for the development of fully controllable photothermal therapies of cancer tumours.

E.1. Core-shell rare-earth-doped nanoparticles for drug delivery.

The use of drug delivery nanosystems has increased enormously due to their enhanced therapeutic efficacy and reduced side effects, derived from their capacity to accurately target the specific area to be treated. Phototriggered-controlled drug-release devices (PDDs) have attracted great attention as they can be activated by light to obtain on-demand release. Light activation allows better spatial and temporal control of drug administration.[93-96] PDDs are based on the encapsulation/linkage of drug molecules inside/to a photoreactive structure which can be “open” by the action of light in order to release the drug molecules when and where needed. Traditional PDDs require UV light for activation. This radiation induces phototoxicity and it shows a limited penetration depth into tissues. Due to these limitations, NIR light activated PDDs are receiving increasing attention in the biological context, since NIR light is able to penetrate deeper into tissue while creating less biological damage. One approach to achieve NIR phototriggered drug release is through the use of NIR-to-UV UC RENPs.[88, 97-100] The design of UC RENP-based PDDs involves the combination of UC RENPs with a drug releaser unit into a single structure. It is in this step where the CS engineering has emerged as a smart solution by using a core constituted by an UC RENP surrounded by a shell that will act as drug releaser.[94, 97, 99-102] When revisiting the literature, β-phase $NaYF_4$:RE@$NaYF_4$ systems emerge as the most popular for constituting the emitting core due to its high IR-to-UV-VIS optical conversion efficiency. [12] Regarding the drug releaser shell, there are two main strategies. The first one consists on the encapsulation of the UC core into a silica coating (UC RENP@SiO_2) or into a polymer (UC RENP@polymer).

SiO_2 encapsulation is commonly used since its surface can be easily functionalized with diverse groups enabling other NPs or photosensitive molecules to attach. Moreover, mesoporous SiO_2 ($mSiO_2$) presents a porous structure (with high surface area), which provides reservoirs for loading drug molecules. By combining CS UCNPs with SiO_2 or $mSiO_2$ outer shells, novel CS nanomaterials for PDDs were obtained.[98, 100, 103] Liu *et al*.[98] reported a strategy for NIR-activated PDDs based on $mSiO_2$-coated UC CS RENPs structure capable of simultaneously emit UV and VIS light. The anticancer drug Doxorubicin (DOX) was loaded into the mesoporous silica shell in addition to photoactive azobencene (azo) molecules. These photoresponsive molecules possess the ability to transit from the *cis* to *trans* isomer (and vice versa) by the absorption of VIS (or UV) light. The reversible photo isomerization by simultaneous UV and VIS light emitted by the UCNPs creates a continuous rotation-inversion movement of the azo molecules, which acts as a molecular impeller that drives the release of DOX molecules. The authors also demonstrated an *in vitro* controlled NIR-triggered drug delivery experiment.

A similar approach was followed by He *et al*.,[100] who developed a PDD based on a photosensitive ruthenium complex, which was used to shield the $mSiO_2$ pores where DOX molecules were stored. They designed the UCNP@$mSiO_2$ structure in order to maximize the UV emission, which overlaps with the absorption of the photosensitive complex. When activated, the Ru complexes act as molecular valves which allow the release of the drug molecules. Thanks to the developed PDD, these authors reported the lowest laser excitation power density at 980 nm ever used for UC RENP-assisted drug delivery (0.35 Wcm^{-2}), which minimizes the overheating effect and photodamage produced by that wavelength.

In the case of UCNP@polymer structures, UC CS RENPs organic polymers are employed as outer coating in order to load or link the drugs to the nanocarrier by means of self-assembly. Commonly used polymers are PEG, TWEEN, and PEI, among others.[93, 102, 104] Recently, Deng *et al*.[102] designed, synthetized, and tested a novel aptamer-guided nanocarrier based on an UC RENP@polymer able to simultaneously perform targeted pH-triggered drug delivery and bioimaging. Another example is the multifunctional drug delivery system developed by Dai *et al*.[104] which combines UC luminescence, MRI, and CT multimodal bioimaging with NIR-activated platinum drug delivery, taking advantage of CS engineering. They applied the developed nanostructure to inhibit the growth of cancer tumours in animal models by using 980 nm radiation and the subsequent drug release. This multifunctional system can furthermore provide complete information to guide the cancer treatment since it can act as contrast agent for diverse imaging techniques.

In addition to the two architectures described above, CS structures based on UC RENPs can be used to produce rattle-type (denoted as yolk–shell, YS) nanocarriers, as those shown in Figure 9). YSs are a special class of CS nanostructures with core@void@shell structure and tunable functionalities in both the cores and the hollow shell.[101, 105-108] In this case, it is important to mention that core and shell units are not in physical contact. For the purpose of drug delivery, the main advantage of YS CSNPs is that the hollow cavity can endow the overall structure with a huge loading capacity. Zhang *et al*.[101] synthetized a multifunctional YS structure consisting in a UC RENPs shell with a SiO_2-coated Fe_3O_4 core. This structure emits VIS luminescence upon NIR excitation, and it can be manipulated using an external magnetic field to localize it at a specific target, at the same time, it can be used as UC imaging agent. Moreover, they demonstrated the usefulness of the YS structure as anticancer PDDs by loading the structure with DOX. Zhang *et al*.[101] demonstrated antitumour action in animal models by enhancing tumour targeting by the application of a magnetic field.

Another interesting study was performed by Zhao *et al*.[94]. In this case, as it is shown in Figure 9a, the ACCh pro-drug is encapsulated inside a SiO_2 sphere that shells a single UCP that acts as the yolk. Figure 9c shows a TEM image of the structures. Under 980 nm excitation, the UV emission produced by Tm^{3+} ions in the UCNP effectively activate the photolysis of the pro-drug (Figure 9b) that leads to the release of the anticancer drug (ACCh) which diffuses out of the YS UC RENPs through the pores of the silica shell. The tumour growth and mouse survival rates were monitored after the treatment with the developed PDD. PDD-treated tumours showed a much slower growth rate in comparison with the control group (treated with saline and YS structure without Tm^{3+} ions as activators), as shown in

Figure 9. (a) Schematic illustration of the NIR-regulated UC-bases PDD, (b) photolysis of the pro-drug under UC emission from the YS UCNPs. (c) TEM image of the YS UCNPs. (d) Normalized tumor volume in mice intratumoral injected with saline, YS LnNP-ACCh and YS UCNP-ACCh on the 1st day and on the 9th day. In all mice groups, the tumors were exposed to 980 nm laser (50 mW cm^{-2}) for 20 min each day for 16 days. Reproduced with permission from [94]. Copyrigth 2014, Wiley-VCH Verlag GmbH & Co. KGaA.

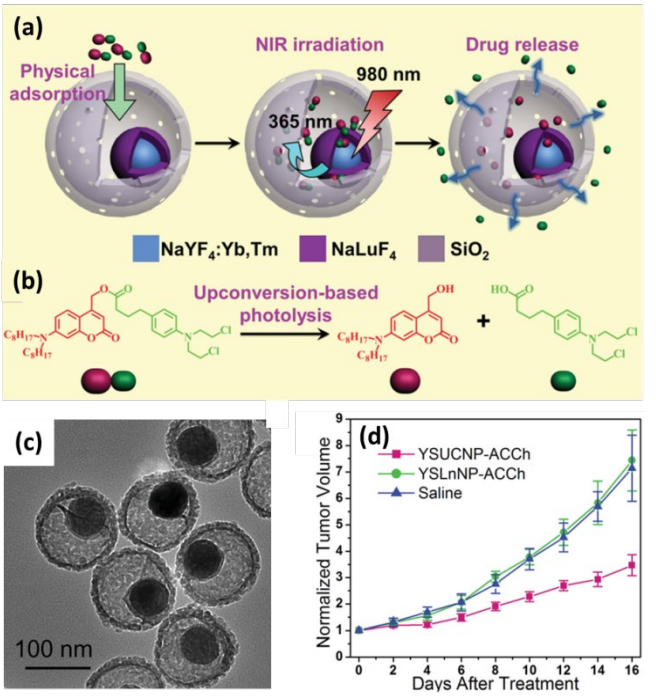

Figure 9d. In addition, the survival time of mice after the administration of the YS UCNP-ACCh PDD was drastically prolonged, indicating the efficiency of the treatment.

E.2. Core-shell rare-earth-doped nanoparticles for photoactivation therapies.

The discovery of PDDs capabilities set off a new research line aiming the development of a new group of therapies: the so-called photoactivation (PAC) based therapies. Here PAC refers to the phenomenon by which molecules (sensitizers) are activated through the absorption of light. Then, these activated molecules can either produce or trigger the production of chemical species which have an effect on biological systems. The main difference between PAC-based systems and PDDs is that, in the first case, the activated molecule has the therapeutic effect itself while, in the second, the sensitizer is used to release the chemical species that has the therapeutic functionality.

In analogy with the systems discussed in Section E.1, the sensitizers used in PAC-based systems are traditionally activated with UV or VIS radiation. Thus the use of optical systems capable of NIR-to-UV/VIS conversion is desirable in order to avoid the drawbacks of UV/VIS excitation. As in previous sections, a nice solution is the use an UC RENP as core/emitting unit.[109] For the activation of the sensitizer, energy must be transferred between the UC RENPs and the molecules. Energy transfer between the UC RENP (donor) and the sensitizer (acceptor) is only possible if the emission band of the former overlaps with the absorption band(s) of the target molecule (as exemplified in the graphs of Figure 10a). Moreover, the efficiency of this energy transfer decreases as the distance between the donor and the acceptor increases, thus the separation between them must be minimized.[110] Even when activation of endogenous sensitizers can be performed,[111, 112] the best strategy to ensure good energy transfer is to coat the UC RENP with the target molecules, embedding them in an outer mesoporous shell, or encapsulating them inside a rattle or YS structure. Li *et al*.[113] demonstrated the possibility of producing core-multishell RENPs which can be excited by two different wavelengths leading to double emission band that, in turn, can separately be employed for the activation of distinct molecules (see Figure 10a). The blue emission of Tm^{3+} ions, obtained under 980 nm excitation, produced the structural transformation of azo molecules. At the same time, the green emission from Er^{3+} ions, obtained under 796 nm excitation, triggered the activation of rose bengal sensitizer. This proof of concept opens the possibility of developing advanced treatments which combine different therapies. In this case, azo molecules act as impellers for drug delivery in chemotherapy treatments, as explained in section E.1. In addition, rose bengal can be used for photodynamic therapies, as explained later on in this section. In addition, since the activation of the molecule only occurs at short range, highly localized therapies can be developed.[114] Special care must be taken when designing the composition and thickness of the different layers. The interlayer thickness, usually employed for UC efficiency enhancement, must not compromise the energy transfer efficiency due to the increase in the distance between the emitting ions and the sensitizer, therefore a compromise must be found.[115, 116] Ding *et al*.[116] theoretically and experimentally demonstrated that an optimization of the energy transfer between the UC RENP and the sensitizer can be achieved by the proper shell thickness.

As a special case of relevance within the field of PAC-assisted therapy, photodynamic therapy (PDT) should be commented in detail. PDT is based on the use of two, in principle, non-toxic agents (i.e. light and sensitizer, such as porphyrin compounds or titania) that, when combined, can produce deleterious effects in cells and tissues.[117] In PDT, the sensitizer, after its light activation, transfers energy to molecular oxygen naturally present in the tissue to generate reactive oxygen species, such as singlet oxygen and, by continuation, radicals, which damage the cells. Recently published works have evidenced the superior *in vitro* PDT performance of CS structures.[118] Among the different CS structures used for PDT, those involving UC cores emerged as the most promising one for both *in vitro*[106, 111, 113, 119, 120] and *in vivo*[121-123]. As in previous cases, this is so because of the possibility of activating them with NIR light. In this sense, the work reported by Hou *et al*.[121] should be highlighted. They developed dual sensitizer core-multishell RENPs. In this structure the core was constituted by an UC RENP and it was in charge of NIR-to-VIS conversion. The closest shell was designed as a spacer between the UC core and the outset shell (containing the sensitizers). This spacing shell was introduced in the structure in order to enhance both the UC efficiency and the energy transfer from the emitting core and the sensitizer. The benefits of this spacing shell were demonstrated by the authors through achieving efficient in vivo treatment of tumours by PDT.

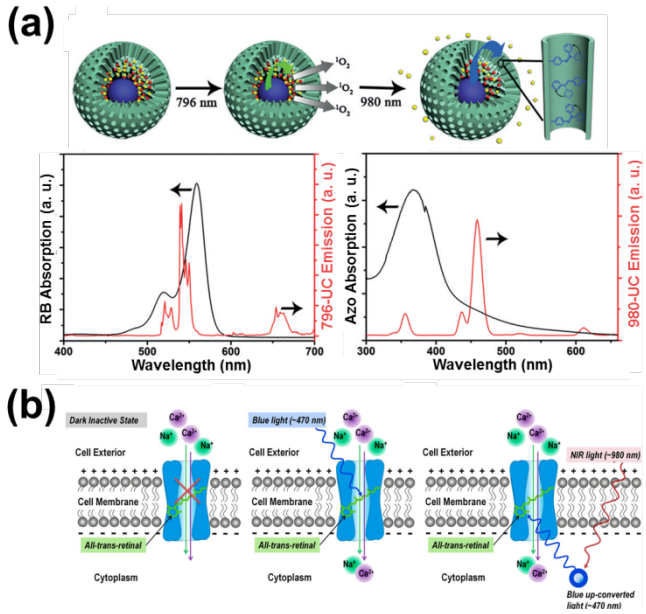

Figure 10. (a) Dual sensitizer core-multishell platform. 796 nm excitation promotes green emission from Er^{3+} ions which matches the absorption of rose bengal for PDT (left diagram and graph), while after 980 nm excitation blue emission of Tm^{3+} ions is produced which matches azo absorption for its activation (right diagram and graph). Reproduced with permission from [113]. Copyright 2016 Wiley-VCH Verlag GmbH & Co. (b) Photoactivation of a optogenetic protein channel by means of direct blue excitation (centre) and UC emission from core-shell UC nanoparticles internalized by the cell (right). Reproduced with permission from [114]. Copyright 2017 American Chemical Society.

Other photochemo-therapies have been developed based on the selective photo-activation of certain molecules also employing CS UC RENPs.[123] For example, carbon monoxide is produced by cells which possess cytoprotective and anti-inflammatory properties. Photoactivated carbon monoxide precursors, termed as photoCORM, have been developed in combination with CS UC RENPs for different therapeutic applications.[124, 125] PAC of anticancer metal complexes by CS UC RENPs was also demonstrated.[126]

Finally, PAC can also be used to influence or control intracellular structures, processes, and molecules. CS structures have indeed been used as activating agents in optogenetics experiments. These are based on the ability of light to control signal transmission and generation processes in neurons. Traditionally, the performances of optogenetics experiments require the incorporation of light-gated ion channels proteins (opsins) into neurons. Cellular signalling can then be activated or supressed through the selectivity opening or closing of these channels by using light. Pliss *et al.*[114] demonstrated efficient control of optogenetic protein channels embedded in the cell membranes by employing the blue light generated by internalized CS UC RENPs after excitation with 975 nm radiation (see Figure 10b). They also observed that PAC only occurred in the vicinity of the CS UC RENPs, thus higher spatial precision was achieved when using the CS UC RENPs in comparison with direct blue light excitation of the channels.

E.3. Core-shell rare earth-doped nanoparticles for photothermal therapies

Thermal therapies are based on the selective heating of cancer cells or pathogenic tissues until they suffer irreversible damage, i.e. due to the advent of hyperthermia.[127-129] NP-assisted thermal therapies, such as magnetic hyperthermia or photothermal therapies (PTTs), consist in the use of NPs as local heaters. In particular, PTTs employ light-activated heating NPs, i.e. NPs capable of efficient light-to-heat conversion.[130] Gold NPs, carbon-based particles, and a variety of organic molecules, among others, have been extensively studied as efficient photothermal agents.[75, 130-132] Traditionally, core-only structures were employed but this is changing towards the use of CS structures as they have been demonstrated as key materials to improve the selectivity and control of PTTs.

In a pioneer study, Zhu *et al.*[51] combined the emission enhancement of the temperature-sensitive luminescent core due to an inert shell with an outer carbon shell acting as heating unit to build a self-monitored nanoheater (see Figure 11a). This system was tested *in vivo* showing good results in the application of localized heat for the reduction of subcutaneous tumours size, as it is shown in Figure 11b and 11c. However, the excitation at 980 nm (leading to non-selective heating due to tissue absorption) and the emission of the temperature-sensitive luminescent ions in the VIS range (both out of the biological windows) make the clinical use of this system unviable. Moreover, the need of different wavelengths for the excitation of the temperature-sensitive luminescent core and the heating shell adds an extra difficulty.

In order to overcome the drawbacks presented by the former structures, an alternative self-monitored nanoheater based only on CS RENPs was proposed by Ximendes *et al.*[60] The performance of the LaF_3:Er,Yb@LaF_3:Nd CS RENPs as self-monitored nanoheaters was compared with that of homogeneously doped LaF_3:Er,Yb,Nd RENPs to prove the benefits of using a CS structure in PTTs. The highly doped shell acts as both an 808 nm excited sensitizer and as a nanoheating unit. Relevant light-to-heat conversion efficiencies at the core were achieved thanks to the high Nd^{3+} dopant levels that result in a large energy diffusion and cross relaxation processes that enhance the overall non-radiative decay probabilities. The core units (doped with Yb^{3+} and Er^{3+} ions) behave as a thermal sensing unit by using the emission generated by the Er^{3+} thermalized levels for remote temperature reading, as Figure 11d schematizes. In this particular structure, the optical activation of both heating and sensing units was, for the first time, obtained under single wavelength excitation. At this point it is important to mention that the CS structure was necessary in order to separate Er^{3+} from Nd^{3+} ions to avoid the quenching of the emission of the former, as shown in Figure 11e. At the same time, the CS structure also avoids the reduction of the pump-to-heat conversion of Nd^{3+} ions due to energy transfer to Er^{3+} ions (see Figure 11f). The potential application of this system for controlled PTTs was tested in an *ex vivo* experiment. Full thermal control during a single beam PTT procedure was demonstrated by Ximendes *et al.* who, at the same time, claimed that further transfer into *in vivo* applications would require the use of sensing ions different from the VIS-emitting Er^{3+} ions in order to achieve larger penetration depths into tissues.

A similar system was proposed by Tong *et al*. [133] employing Sm^{3+} ions as heating centres. As in the structure developed by Ximendes *et al.*, the heating agent is placed in the core and the thermal sensitive Er^{3+} ions are allocated at the shell. Tong and co-workers also demonstrated the potential of these CS structures for fully controlled PTT, but with the limitation of using an excitation wavelength lying outside of the biological windows.

The transfer to clinic of the above mentioned examples of CS RENPs is limited due to the poor penetration depth of the VIS Er^{3+} emission into tissues. This problem can be partially overcome by shifting the excitation wavelengths to the biological windows of transparency.[58] A further and effective improvement would consist in increasing the net absorption of the excitation radiation, which could lead to a larger pump-to-heat conversion and to an increment in the total Er^{3+} emission intensity. This possible solution was explored by Shao *et al.*[134] through the sensitization of the $NaYF_4$:Yb,Er@$NaYF_4$:Yb,Nd@dye CS RENPs by means of NIR absorbing dye molecules (the so-called IR-806). These molecules efficiently absorb 808 nm excitation and their emission overlaps

Figure 11. CS RENPs for PTTs. (a) TEM image of $NaLuF_4$:Yb,Er@$NaLuF_4$@Carbon CS RENPs. Inset: schematic diagram of the CS structure. (b) Thermal images of nude mice with (left panel) and without (right panel) CS RENPs-labelled HeLa cell tumours (top panel) before and (bottom panel) after 3 minutes under 730 nm irradiation (0.3 W cm^{-2}). (c) Representative optical images of nude mice before and after treatment with CS RENPs-labelled HeLa cells under 730 nm irradiation (0.3 W cm^{-2}). Reprinted with permission from [51]. Copyright 2016 Nature Publishing Group. (d) Schematic diagram of the structure and the performance of the LaF_2:Er,Yb@LaF_2:Nd nanoparticles as self-monitored nanoheaters. (e) Normalized intensity decay from the Er^{3+} $^4S_{3/2}$ energy level for different NP structures under excitation at 488 nm. (f) Heating produced by laser excitation at 808 nm for different nanoparticle structures. Dots are experimental data and dashed lines the best the linear fit. Inset: Thermal images of the diverse nanoparticle structures under the highest excitation power. Reprinted with permission from [60]. Copyright 2016 Royal Society of Chemistry.

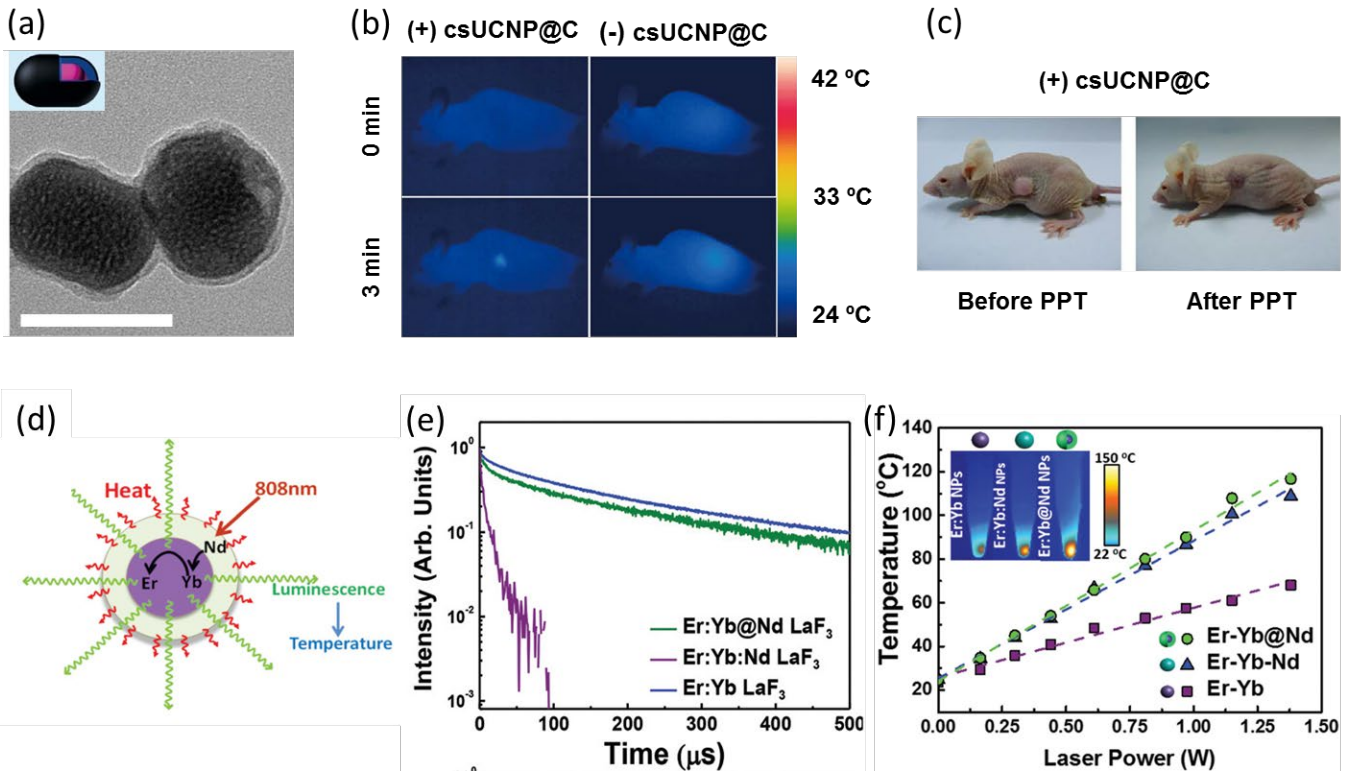

with the absorption band of Nd^{3+} ions. So that the RE ions are excited thanks to dye-to-neodymium energy transfer. Shao and co-workers demonstrated how CS NPs functionalized with these dye molecules shows a 28-fold enhancement in Er^{3+} emission intensity and about triple induced temperature rise.[134] As stated in Section C.2, dye-sensitizing strategy is leading to relevant and numerous advances in several fields of application of RE-doped luminescent materials.

In addition to the solution proposed by Shao *et al.*, an interesting alternative solution was later demonstrated by Ximendes *et al.*[135] As explained in section D, they designed and developed LaF_3:Yb@LaF_3:Nd CS RENPs. In this case, the heating ions (Nd^{3+}) were placed at the shell and the thermal reading was achieved by monitoring the temperature-dependent $Nd^{3+} \rightarrow Yb^{3+}$ energy transfer in the CS interface. The excitation and the emission of this self-monitored nanoheater in the first and second biological windows of transparency, respectively, allowed to study real time *ex vivo* subcutaneous heating process, obtaining good estimations for the depth of the self-monitored nanoheaters and proving their potential application in *in vivo* controlled PTT.

Taking another step forward in the control of PTTs, Marciniak *et al*.[136] proposed CS RENPs as self-monitored nanoheaters, which uses Nd^{3+} ions not only as heating agents (stoichiometric core), but also as temperature sensors and imaging source (slightly doped outer shell). The non-doped interlayer avoids cross-relaxations between Nd^{3+} ions, increasing the quantum efficiency of the system. These authors suggested an excitation strategy to accurately select the volume of tissue to be treated and so avoid collateral damages, as NPs may distribute in specimens further from the zones to be treated. This is based on combining two laser beams with intensity lower than that of the threshold for producing hyperthermia, which overlap in the treated zone achieving a total intensity enough to rise temperature at the typical values of PTTs.

F. CONCLUSIONS AND PERSPECTIVES

In summary, we have examined the diverse CS RENPs that have already been used for biomedical purposes. This review article demonstrates that, although a lot of work has been done, this research field is, in our opinion, writing its first pages. The fast development of this area is clearly a consequence of the improvement in the techniques for synthesis that allowed the fabrication of high quality CS structures. Examples provided herein evidence that almost any imaginable structure can be synthetized.

Among the different achievements described in this review, we think that three of them will have a great impact in the field of nanomedicine. The first one is the use of CS architectures in combination with dopant engineering to minimize undesirable thermal loading produced by the excitation source during imaging or sensing experiments. In this sense, neodymium ion is the most promising ion capable of efficient absorption at around 800 nm, where tissue absorption is minimum and the most cost-effective laser diodes work. Secondly, CS structures also made an old dream possible: the fabrication of a single system capable of simultaneous heating and thermal sensing. This allowed the development of minimally invasive thermal therapies activated either by light or by alternating magnetic fields. Finally, this review discussed how CS RENPs are starting to be used for *in vivo* studies aimed to alter the behaviour through the control of the brain. These last results demonstrated that the area of application of CS RENPs is not restricted to imaging or therapy but, indeed, these structures may become an indispensable and flexible tool for researchers working in the frontiers of knowledge.

We have shown that CS RENPs have been widely used for photo-activated therapies based on drug release or drug activation. In most cases, UC RENPs that transform IR light into VIS or UV radiation (the latter being used as activating energy source) are employed. Despite the good results obtained so far in this area we are of the opinion that further optimization is still required. In particular, the quantum efficiency of UC processes in RENPs is typically very low (below 1%) so that the overall efficiency of the structures based on them is limited. In addition, CS RENPs have also the inherent drawback of the low absorption cross section characteristic of these ions (several orders of magnitude lower than those of quantum dots, for instance). Overcoming these limitations will be one of the challenges that the scientific community should face in the near future. Possible solutions could be found by exploring the synthesis of heavily doped structures with reduced quenching. This could be achieved by avoiding, for instance, cross relaxation and energy migration processes.

CS RENPs have also been demonstrated to be promising probes for multimodal bioimaging. An adequate design has made possible the simultaneous acquisition of *in vivo* images by using different techniques such as X-Ray, luminescence, and MRI. The results obtained in this field are interesting and very attractive from a fundamental point of view. Nevertheless, in our opinion the actual advantage of obtaining simultaneous multimodal bioimages is not yet clearly demonstrated. We believe that some examples showing the positive synergy between these techniques should be given to convince the scientific community that the research on multimodal structures is worth the effort. For instance, we believe that these multimodal structures should be used for advanced and precise diagnosis in the near future to demonstrate that this research line is not just a fleeting fashion.

In addition, CS engineering has demonstrated to be a very efficient strategy for tailoring the fluorescence lifetime of CS RENPs. In our opinion, this possibility offers more than just the development of high brightness structures (useful for the achievement of

high contrast *in vivo* images). We are firmly convinced that lifetime tailoring will allow the use of such structures in advanced imaging based on time-domain analysis.

Finally we would like to remark that the future use of CS RENPs for *in vivo* studies mainly relies on the development of nanostructures emitting within the second biological window of transparency of tissues (emissions in the 1000-1350 nm range). Therefore, we state that new combinations of RE ions should be explored to find a new nanostructures which presents intense and sensitive emission in this range under 800 nm excitation (fist biological window). Although some CS RENPs satisfying these requirements have already been presented (see Section D1), their brightness and efficiency are far from being high enough to ensure a successful transfer to the clinic. We also reckon that, in the near future, most of the commercial small animal imaging apparatuses will be equipped with broad band IR LED source instead of narrow-line laser diodes. This would boost the use of CS RENPs with broad absorption bands in the IR region. Therefore, we think that both inhomogeneous line broadened RE-doped systems and dye-sensitized RENPs could emerge with great potential.

To conclude, CS RENPs are, without any doubt, promising systems for advanced diagnosis and therapy applications. Nevertheless, this research area is still in an early stage, since, for example, overcoming the challenge of moving into the clinic will require an intense work in complementary areas such as material sciences, optical engineering, and nanobiology.

Conflicts of interest

There are no conflicts to declare.

Acknowledgements

This work has been partially supported by the Ministerio de Economía y Competitividad de España (MINECO) (MAT2016-75362-C3-1-R), by the Instituto de Salud Carlos III (PI16/00812), by the Comunidad Autónoma de Madrid (B2017/BMD-3867RENIM-CM), by the European Comission (NanoTBTech), and "cofinanciado con Fondos Estructurales de la Union Europea". This work has been also partially supported by COST action CM1403. L.L.P. thanks the Universidad Autónoma de Madrid for the "Formación de personal investigador (FPI-UAM)" program. P.R.S. thanks MINECO and the Fondo Social Europeo (FSE) for the "Promoción del talento y su Empleabilidad en I+D+i" statal program (BES-2014-069410). D.H.O. is grateful to the Instituto de Salud Carlos III for a Sara Borrell Fellowship (CD17/00210).

Notes and references

1. Y. Liu, H. Miyoshi and M. Nakamura, *International Journal of Cancer*, 2007, **120**, 2527-2537.
2. K. Riehemann, S. W. Schneider, T. A. Luger, B. Godin, M. Ferrari and H. Fuchs, *Angewandte Chemie International Edition*, 2009, **48**, 872-897.
3. R. A. Sperling and W. J. Parak, *Philosophical Transactions of the Royal Society A: Mathematical, Physical and Engineering Sciences*, 2010, **368**, 1333-1383.
4. X. H. Gao, Y. Y. Cui, R. M. Levenson, L. W. K. Chung and S. M. Nie, *Nature Biotechnology*, 2004, **22**, 969-976.
5. C. Li, Y. Zhang, M. Wang, Y. Zhang, G. Chen, L. Li, D. Wu and Q. Wang, *Biomaterials*, 2014, **35**, 393-400.
6. X. Michalet, F. F. Pinaud, L. A. Bentolila, J. M. Tsay, S. Doose, J. J. Li, G. Sundaresan, A. M. Wu, S. S. Gambhir and S. Weiss, *Science*, 2005, **307**, 538-544.
7. R. Y. Tsien, *Annual Review of Biochemistry*, 1998, **67**, 509-544.
8. G. Wakefield, H. A. Keron, P. J. Dobson and J. L. Hutchison, *Journal of Colloid and Interface Science*, 1999, **215**, 179-182.
9. H. Dong, S.-R. Du, X.-Y. Zheng, G.-M. Lyu, L.-D. Sun, L.-D. Li, P.-Z. Zhang, C. Zhang and C.-H. Yan, *Chemical reviews*, 2015, **115**, 10725-10815.
10. F. Vetrone and J. A. Capobianco, *International Journal of Nanotechnology*, 2008, **5**, 1306-1339.
11. A. Gnach and A. Bednarkiewicz, *Nano Today*, 2012, **7**, 532-563.
12. F. Wang and X. Liu, *Chemical Society Reviews*, 2009, **38**, 976-989.
13. V. Mahalingam, F. Vetrone, R. Naccache, A. Speghini and J. A. Capobianco, *Advanced Materials*, 2009, **21**, 4025-4028.
14. F. Vetrone, R. Naccache, V. Mahalingam, C. G. Morgan and J. A. Capobianco, *Advanced Functional Materials*, 2009, **19**, 2924-2929.
15. R. D. Averitt, D. Sarkar and N. J. Halas, *Physical Review Letters*, 1997, **78**, 4217-4220.
16. Z. Cui and Z. Zhang, *Nanostructured Materials*, 1996, **7**, 355-361.
17. M. A. Correa-Duarte, M. Giersig and L. M. Liz-Marzán, *Chemical Physics Letters*, 1998, **286**, 497-501.
18. J. L. Turner, D. Pan, R. Plummer, Z. Chen, A. K. Whittaker and K. L. Wooley, *Advanced Functional Materials*, 2005, **15**, 1248-1254.
19. H. Lu, G. Yi, S. Zhao, D. Chen, L.-H. Guo and J. Cheng, *Journal of Materials Chemistry*, 2004, **14**, 1336-1341.
20. J. W. Stouwdam and F. C. J. M. van Veggel, *Langmuir*, 2004, **20**, 11763-11771.
21. J. R. DiMaio, C. Sabatier, B. Kokuoz and J. Ballato, *Proceedings of the National Academy of Sciences*, 2008, **105**, 1809-1813.
22. C. F. Gainer and M. Romanowski, *Journal of Innovative Optical Health Sciences*, 2014, **7**, 1330007.

23. X. Li, F. Zhang and D. Zhao, *Chem. Soc. Rev.*, 2015, **44**, 1346-1378.
24. Y. Liu, D. Tu, H. Zhu and X. Chen, *Chem. Soc. Rev.*, 2013, **42**, 6924-6958.
25. R. Naccache, Q. Yu and J. A. Capobianco, *Adv. Opt. Mater.*, 2015, **3**, 482-509.
26. J. Zhou, Q. Liu, W. Feng, Y. Sun and F. Li, *Chemical reviews*, 2014, **115**, 395-465.
27. C. Caltagirone, A. Bettoschi, A. Garau and R. Montis, *Chemical Society Reviews*, 2015, **44**, 4645-4671.
28. A. L. Feng, M. L. You, L. Tian, S. Singamaneni, M. Liu, Z. Duan, T. J. Lu, F. Xu and M. Lin, *Scientific Reports*, 2015, **5**, 7779.
29. L. P. Qian, L. H. Zhou, H.-P. Too and G.-M. Chow, *Journal of Nanoparticle Research*, 2010, **13**, 499-510.
30. X. Zhang, B. Li, M. Jiang, L. Zhang and H. Ma, *RSC Advances*, 2016, **6**, 36528-36533.
31. M. Fujii, T. Nakano, K. Imakita and S. Hayashi, *J. Phys. Chem. C*, 2013, **117**, 1113-1120.
32. L. Song, N. Zhao and F.-J. Xu, *Advanced Functional Materials*, 2017, **27**, 1701255-n/a.
33. D. Chen and Y. Wang, *Nanoscale*, 2013, **5**, 4621-4637.
34. F. Vetrone, R. Naccache, V. Mahalingam, C. G. Morgan and J. a. Capobianco, *Adv. Funct. Mater.*, 2009, **19**, 2924-2929.
35. X. Li, D. Shen, J. Yang, C. Yao, R. Che, F. Zhang and D. Zhao, *Chemistry of Materials*, 2013, **25**, 106-112.
36. X. Li, R. Wang, F. Zhang and D. Zhao, *Nano Letters*, 2014, **14**, 3634-3639.
37. M. Quintanilla, F. Ren, D. Ma and F. Vetrone, *ACS Photonics*, 2014, **1**, 662-669.
38. N. J. J. Johnson, A. Korinek, C. Dong and F. C. J. M. van Veggel, *Journal of the American Chemical Society*, 2012, **134**, 11068-11071.
39. H. Jiang, Z. Sun, Z. Liu, P. Cheng, X. Liu, J. Sun and L. Liu, *Materials Research Bulletin*, 2018, **101**, 61-66.
40. K. Korthout, P. F. Smet and D. Poelman, *Applied Physics Letters*, 2011, **98**, 261919.
41. X. Chen, L. Jin, W. Kong, T. Sun, W. Zhang, X. Liu, J. Fan, S. F. Yu and F. Wang, *Nature Communications*, 2016, **7**, 10304.
42. J. A. Damasco, G. Chen, W. Shao, H. Agren, H. Huang, W. Song, J. F. Lovell and P. N. Prasad, *Acs Applied Materials & Interfaces*, 2014, **6**, 13884-13893.
43. X. Li, R. Wang, F. Zhang, L. Zhou, D. Shen, C. Yao and D. Zhao, *Scientific Reports*, 2013, **3**.
44. G. Tian, W. Yin, J. Jin, X. Zhang, G. Xing, S. Li, Z. Gu and Y. Zhao, *Journal of Materials Chemistry B*, 2014, **2**, 1379-1389.
45. Y. Huang, Q. Xiao, H. Hu, K. Zhang, Y. Feng, F. Li, J. Wang, X. Ding, J. Jiang, Y. Li, L. Shi and H. Lin, *Small*, 2016, **12**, 4200-4210.
46. J. Shen, G. Chen, T. Y. Ohulchanskyy, S. J. Kesseli, S. Buchholz, Z. Li, P. N. Prasad and G. Han, *Small*, 2013, **9**, 3213-3217.
47. L. Liang, X. Xie, D. T. B. Loong, A. H. All, L. Huang and X. Liu, *Chemistry-a European Journal*, 2016, **22**, 10801-10807.
48. G. Chen, J. Shen, T. Y. Ohulchanskyy, N. J. Patel, A. Kutikov, Z. Li, J. Song, R. K. Pandey, H. Agren, P. N. Prasad and G. Han, *ACS Nano*, 2012, **6**, 8280-8287.
49. G. Chen, T. Y. Ohulchanskyy, S. Liu, W.-C. Law, F. Wu, M. T. Swihart, H. Agren and P. N. Prasad, *ACS Nano*, 2012, **6**, 2969-2977.
50. Y. Zhong, Z. Ma, S. Zhu, J. Yue, M. Zhang, A. L. Antaris, J. Yuan, R. Cui, H. Wan, Y. Zhou, W. Wang, N. F. Huang, J. Luo, Z. Hu and H. Dai, *Nat. Commun.*, 2017, **8**.
51. X. Zhu, W. Feng, J. Chang, Y.-W. Tan, J. Li, M. Chen, Y. Sun and F. Li, *Nat. Commun.*, 2016, **7**.
52. M. Zheng, C. Yue, Y. Ma, P. Gong, P. Zhao, C. Zheng, Z. Sheng, P. Zhang, Z. Wang and L. Cai, *Acs Nano*, 2013, **7**, 2056-2067.
53. L. Labrador-Páez, M. Pedroni, K. Smits, A. Speghini, F. Jaque, J. García-Solé, D. Jaque and P. Haro-González, *Particle & Particle Systems Characterization*, 2017, DOI: 10.1002/ppsc.201700276.
54. W. Fan, B. Shen, W. Bu, F. Chen, K. Zhao, S. Zhang, L. Zhou, W. Peng, Q. Xiao, H. Xing, J. Liu, D. Ni, Q. He and J. Shi, *J. Am. Chem. Soc.*, 2013, **135**, 6494-6503.
55. Z. Wang, P. Zhang, Q. Yuan, X. Xu, P. Lei, X. Liu, Y. Su, L. Dong, J. Feng and H. Zhang, *Nanoscale*, 2015, **7**, 17861-17870.
56. Q. Xiao, W. Bu, Q. Ren, S. Zhang, H. Xing, F. Chen, M. Li, X. Zheng, Y. Huab, L. Zhou, W. Peng, H. Qu, Z. Wang, K. Zhao and J. Shi, *Biomaterials*, 2012, **33**, 7530-7539.
57. P. Haro-Gonzalez, W. T. Ramsay, L. Martinez Maestro, B. del Rosal, K. Santacruz-Gomez, M. del Carmen Iglesias-de la Cruz, F. Sanz-Rodriguez, J. Y. Chooi, P. Rodriguez Sevilla, M. Bettinelli, D. Choudhury, A. K. Kar, J. Garcia Sole, D. Jaque and L. Paterson, *Small*, 2013, **9**, 2162-2170.
58. E. Hemmer, A. Benayas, F. Légaré and F. Vetrone, *Nanoscale Horizons*, 2016, **1**, 168-184.
59. L. Zeng, Y. Pan, R. Zou, J. Zhang, Y. Tian, Z. Teng, S. Wang, W. Ren, X. Xiao, J. Zhang, L. Zhang, A. Li, G. Lu and A. Wu, *Biomaterials*, 2016, **103**, 116-127.
60. E. C. Ximendes, U. Rocha, C. Jacinto, K. U. Kumar, D. Bravo, F. J. López, E. M. Rodríguez, J. García-Solé and D. Jaque, *Nanoscale*, 2016, **8**, 3057-3066.
61. Y.-F. Wang, G.-Y. Liu, L.-D. Sun, J.-W. Xiao, J.-C. Zhou and C.-H. Yan, *ACS Nano*, 2013, **7**, 7200-7206.
62. Y. Li, J. Tang, D.-X. Pan, L.-D. Sun, C. Chen, Y. Liu, Y.-F. Wang, S. Shi and C.-H. Yan, *ACS Nano*, 2016, **10**, 2766-2773.
63. W. Shao, G. Chen, A. Kuzmin, H. L. Kutscher, A. Pliss, T. Y. Ohulchanskyy and P. N. Prasad, *J. Am. Chem. Soc.*, 2016, **138**, 16192-16195.
64. X. Wu, Y. Zhang, K. Takle, O. Bilsel, Z. Li, H. Lee, Z. Zhang, D. Li, W. Fan and C. Duan, *ACS Nano*, 2016, **10**, 1060-1066.
65. B. E. Hardin, H. J. Snaith and M. D. McGehee, *Nat. Photonics*, 2012, **6**, 162.
66. Y. Sun, X. Zhu, J. Peng and F. Li, *ACS Nano*, 2013, **7**, 11290-11300.
67. J.-W. Shen, C.-X. Yang, L.-X. Dong, H.-R. Sun, K. Gao and X.-P. Yan, *Anal. Chem.*, 2013, **85**, 12166-12172.
68. Y. Wang, S. Song, J. Liu, D. Liu and H. Zhang, *Angew. Chem., Int. Ed.*, 2015, **54**, 536-540.
69. R. Lv, P. Yang, F. He, S. Gai, G. Yang, Y. Dai, Z. Hou and J. Lin, *Biomaterials*, 2015, **63**, 115-127.
70. R. Lv, P. Yang, G. Chen, S. Gai, J. Xu and P. N. Prasad, *Scientific Reports*, 2017, **7**.
71. Y. I. Park, J. H. Kim, K. T. Lee, K.-S. Jeon, H. Bin Na, J. H. Yu, H. M. Kim, N. Lee, S. H. Choi, S.-I. Baik, H. Kim, S. P. Park, B.-J. Park, Y. W. Kim, S. H. Lee, S.-Y. Yoon, I. C. Song, W. K. Moon, Y. D. Suh and T. Hyeon, *Adv. Mater.*, 2009, **21**, 4467-+.

72. D. Ni, J. Zhang, W. Bu, H. Xing, F. Han, Q. Xiao, Z. Yao, F. Chen, Q. He, J. Liu, S. Zhang, W. Fan, L. Zhou, W. Peng and J. Shi, *ACS Nano*, 2014, **8**, 1231-1242.
73. T. Liu, S. Li, Y. Liu, Q. Guo, L. Wang, D. Liu and J. Zhou, *Journal of Materials Chemistry B*, 2016, **4**, 2697-2705.
74. F. He, G. Yang, P. Yang, Y. Yu, R. Lv, C. Li, Y. Dai, S. Gai and J. Lin, *Adv. Funct. Mater.*, 2015, **25**, 3966-3976.
75. F. He, L. Feng, P. Yang, B. Liu, S. Gai, G. Yang, Y. Dai and J. Lin, *Biomaterials*, 2016, **105**, 77-88.
76. J. Rieffel, F. Chen, J. Kim, G. Chen, W. Shao, S. Shao, U. Chitgupi, R. Hernandez, S. A. Graves, R. J. Nickles, P. N. Prasad, C. Kim, W. Cai and J. F. Lovell, *Adv. Mater.*, 2015, **27**, 1785-+.
77. R. Lv, D. Wang, L. Xiao, G. Chen, J. Xia and P. N. Prasad, *Scientific Reports*, 2017, **7**.
78. R. Piñol, C. D. S. Brites, R. Bustamante, A. Martínez, N. J. O. Silva, J. L. Murillo, R. Cases, J. Carrey, C. Estepa, C. Sosa, F. Palacio, L. D. Carlos and A. Millán, *ACS Nano*, 2015, **9**, 3134-3142.
79. E. C. Ximendes, W. Q. Santos, U. Rocha, U. K. Kagola, F. Sanz-Rodríguez, N. Fernández, A. d. S. Gouveia-Neto, D. Bravo, A. M. Domingo, B. del Rosal, C. D. S. Brites, L. D. Carlos, D. Jaque and C. Jacinto, *Nano Letters*, 2016, **16**, 1695-1703.
80. E. C. Ximendes, U. Rocha, B. del Rosal, A. Vaquero, F. Sanz-Rodríguez, L. Monge, F. Ren, F. Vetrone, D. Ma, J. García-Solé, C. Jacinto, D. Jaque and N. Fernández, *Advanced Healthcare Materials*, 2017, **6**, 1601195.
81. L. Lévesque, *Biomedical Optics Express*, 2014, **5**, 701.
82. C. A. Perez and S. A. Sapareto, *Cancer Res.*, 1984, **44**, 4818s-4825s.
83. J. W. Valvano, in *Optical-Thermal Response of Laser-Irradiated Tissue*, eds. A. J. Welch and M. J. C. Van Gemert, Springer US, Boston, MA, 1995, pp. 445-488.
84. J. W. Valvano, J. R. Cochran and K. R. Diller, *International Journal of Thermophysics*, 1985, **6**, 301-311.
85. A. Skripka, A. Benayas, R. Marin, P. Canton, E. Hemmer and F. Vetrone, *Nanoscale*, 2017, **9**, 3079-3085.
86. E. C. Ximendes, U. Rocha, T. O. Sales, N. Fernández, F. Sanz-Rodríguez, I. R. Martín, C. Jacinto and D. Jaque, *Advanced Functional Materials*, 2017, **27**, 1702249.
87. R. Vyas and M. L. Rustgi, *Medical Physics*, 1992, **19**, 1319-1324.
88. B. Liu, C. Li, P. Yang, Z. Hou and J. Lin, *Advanced Materials*, 2017, **29**, 1605434-n/a.
89. M. Sy, A. Nonat, N. Hildebrandt and L. J. Charbonnière, *Chem. Commun.*, 2016, **52**, 5080-5095.
90. A. Son, A. Dhirapong, D. K. Dosev, I. M. Kennedy, R. H. Weiss and K. R. Hristova, *Anal. Bioanal. Chem.*, 2008, **390**, 1829-1835.
91. X. Zou, Y. Liu, X. Zhu, M. Chen, L. Yao, W. Feng and F. Li, *Nanoscale*, 2015, **7**, 4105-4113.
92. L. Chen, X. Li, D. Shen, L. Zhou, D. Zhu, C. Fan and F. Zhang, *Anal. Chem.*, 2015, **87**, 5745-5752.
93. D. M. Yang, P. A. Ma, Z. Y. Hou, Z. Y. Cheng, C. X. Li and J. Lin, *Chemical Society Reviews*, 2015, **44**, 1416-1448.
94. L. Z. Zhao, J. J. Peng, Q. Huang, C. Y. Li, M. Chen, Y. Sun, Q. N. Lin, L. Y. Zhu and F. Y. Li, *Advanced Functional Materials*, 2014, **24**, 363-371.
95. N. Fomina, J. Sankaranarayanan and A. Almutairi, *Advanced drug delivery reviews*, 2012, **64**, 1005-1020.
96. D. Peer, J. M. Karp, S. Hong, O. C. Farokhzad, R. Margalit and R. Langer, *Nature Nanotechnology*, 2007, **2**, 751.
97. B. Liu, Y. Chen, C. Li, F. He, Z. Hou, S. Huang, H. Zhu, X. Chen and J. Lin, *Advanced Functional Materials*, 2015, **25**, 4717-4729.
98. J. A. Liu, W. B. Bu, L. M. Pan and J. L. Shi, *Angewandte Chemie-International Edition*, 2013, **52**, 4375-4379.
99. Z. H. Xu, P. A. Ma, C. X. Li, Z. Y. Hou, X. F. Zhai, S. S. Huang and J. Lin, *Biomaterials*, 2011, **32**, 4161-4173.
100. S. Q. He, K. Krippes, S. Ritz, Z. J. Chen, A. Best, H. J. Butt, V. Mailander and S. Wu, *Chemical Communications*, 2015, **51**, 431-434.
101. F. Zhang, G. B. Braun, A. Pallaoro, Y. C. Zhang, Y. F. Shi, D. X. Cui, M. Moskovits, D. Y. Zhao and G. D. Stucky, *Nano Letters*, 2012, **12**, 61-67.
102. K. R. Deng, Z. Y. Hou, X. J. Li, C. X. Li, Y. X. Zhang, X. R. Deng, Z. Y. Cheng and J. Lin, *Scientific Reports*, 2015, **5**.
103. M. K. G. Jayakumar, A. Bansal, K. Huang, R. S. Yao, B. N. Li and Y. Zhang, *Acs Nano*, 2014, **8**, 4848-4858.
104. Y. L. Dai, H. H. Xiao, J. H. Liu, Q. H. Yuan, P. A. Ma, D. M. Yang, C. X. Li, Z. Y. Cheng, Z. Y. Hou, P. P. Yang and J. Lin, *Journal of the American Chemical Society*, 2013, **135**, 18920-18929.
105. L. Zhang, T. Wang, L. Yang, C. Liu, C. Wang, H. Liu, Y. A. Wang and Z. Su, *Chemistry – A European Journal*, 2012, **18**, 12512-12521.
106. S. Lu, D. Tu, P. Hu, J. Xu, R. Li, M. Wang, Z. Chen, M. Huang and X. Chen, *Angewandte Chemie International Edition*, 2015, **54**, 7915-7919.
107. B. Liu, C. Li, P. a. Ma, Y. Chen, Y. Zhang, Z. Hou, S. Huang and J. Lin, *Nanoscale*, 2015, **7**, 1839-1848.
108. X. Zhu, J. Zhou, M. Chen, M. Shi, W. Feng and F. Li, *Biomaterials*, 2012, **33**, 4618-4627.
109. N. M. Idris, M. K. G. Jayakumar, A. Bansal and Y. Zhang, *Chemical Society Reviews*, 2015, **44**, 1449-1478.
110. R. Marin, L. Labrador-Paéz, A. Skripka, P. Haro González, A. Benayas, P. Canton, D. Jaque and F. Vetrone, *ACS Photonics*, 2018.
111. K. E. Mironova, D. A. Khochenkov, A. N. Generalova, V. V. Rocheva, N. V. Sholina, A. V. Nechaev, V. A. Semchishen, S. M. Deyev, A. V. Zvyagin and E. V. Khaydukov, *Nanoscale*, 2017, **9**, 14921-14928.
112. E. V. Khaydukov, K. E. Mironova, V. A. Semchishen, A. N. Generalova, A. V. Nechaev, D. A. Khochenkov, E. V. Stepanova, O. I. Lebedev, A. V. Zvyagin, S. M. Deyev and V. Y. Panchenko, *Scientific Reports*, 2016, **6**, 35103.
113. X. Li, Z. Guo, T. Zhao, Y. Lu, L. Zhou, D. Zhao and F. Zhang, *Angewandte Chemie International Edition*, 2016, **55**, 2464-2469.
114. A. Pliss, T. Y. Ohulchanskyy, G. Chen, J. Damasco, C. E. Bass and P. N. Prasad, *ACS Photonics*, 2017, **4**, 806-814.
115. Y. Wang, K. Liu, X. Liu, K. Dohnalová, T. Gregorkiewicz, X. Kong, M. C. G. Aalders, W. J. Buma and H. Zhang, *The Journal of Physical Chemistry Letters*, 2011, **2**, 2083-2088.
116. Y. Ding, F. Wu, Y. Zhang, X. Liu, E. M. L. D. de Jong, T. Gregorkiewicz, X. Hong, Y. Liu, M. C. G. Aalders, W. J. Buma and H. Zhang, *The Journal of Physical Chemistry Letters*, 2015, **6**, 2518-2523.
117. D. E. J. G. J. Dolmans, D. Fukumura and R. K. Jain, *Nat Rev Cancer*, 2003, **3**, 380-387.
118. J. Wang, Y. Zhong, X. Wang, W. Yang, F. Bai, B. Zhang, L. Alarid, K. Bian and H. Fan, *Nano Letters*, 2017, **17**, 6916-6921.

119. F. Ai, Q. Ju, X. Zhang, X. Chen, F. Wang and G. Zhu, *Scientific Reports*, 2015, **5**, 10785.
120. Y. Chen, R. Tong, N. An, H. Lin and F. Qu, *New Journal of Chemistry*, 2017, **41**, 7292-7301.
121. Z. Hou, K. Deng, C. Li, X. Deng, H. Lian, Z. Cheng, D. Jin and J. Lin, *Biomaterials*, 2016, **101**, 32-46.
122. R. Lv, D. Yang, P. Yang, J. Xu, F. He, S. Gai, C. Li, Y. Dai, G. Yang and J. Lin, *Chemistry of Materials*, 2016, **28**, 4724-4734.
123. Y. I. Park, H. M. Kim, J. H. Kim, K. C. Moon, B. Yoo, K. T. Lee, N. Lee, Y. Choi, W. Park, D. Ling, K. Na, W. K. Moon, S. H. Choi, H. S. Park, S.-Y. Yoon, Y. D. Suh, S. H. Lee and T. Hyeon, *Advanced Materials*, 2012, **24**, 5755-5761.
124. A. E. Pierri, P.-J. Huang, J. V. Garcia, J. G. Stanfill, M. Chui, G. Wu, N. Zheng and P. C. Ford, *Chemical Communications*, 2015, **51**, 2072-2075.
125. J. Ou, W. Zheng, Z. Xiao, Y. Yan, X. Jiang, Y. Dou, R. Jiang and X. Liu, *Journal of Materials Chemistry B*, 2017, **5**, 8161-8168.
126. E. Ruggiero, C. Garino, J. C. Mareque-Rivas, A. Habtemariam and L. Salassa, *Chemistry – A European Journal*, 2016, **22**, 2801-2811.
127. P. Wust, B. Hildebrandt, G. Sreenivasa, B. Rau, J. Gellermann, H. Riess, R. Felix and P. Schlag, *The lancet oncology*, 2002, **3**, 487-497.
128. B. Hildebrandt, P. Wust, O. Ahlers, A. Dieing, G. Sreenivasa, T. Kerner, R. Felix and H. Riess, *Critical reviews in oncology/hematology*, 2002, **43**, 33-56.
129. J. L. Roti Roti, *Int. J. Hyperthermia*, 2008, **24**, 3-15.
130. D. Jaque, L. M. Maestro, B. Del Rosal, P. Haro-Gonzalez, A. Benayas, J. Plaza, E. M. Rodriguez and J. G. Sole, *Nanoscale*, 2014, **6**, 9494-9530.
131. H. Chen, L. Shao, T. Ming, Z. Sun, C. Zhao, B. Yang and J. Wang, *Small*, 2010, **6**, 2272-2280.
132. F. Liu, X. He, Z. Lei, L. Liu, J. Zhang, H. You, H. Zhang and Z. Wang, *Advanced healthcare materials*, 2015, **4**, 559-568.
133. L. Tong, X. Li, J. Zhang, S. Xu, J. Sun, H. Zheng, Y. Zhang, X. Zhang, R. Hua and H. Xia, *Optics Express*, 2017, **25**, 16047-16058.
134. Q. Shao, X. Li, P. Hua, G. Zhang, Y. Dong and J. Jiang, *J. Colloid Interface Sci.*, 2017, **486**, 121-127.
135. E. Clayton Ximendes, U. Rocha, K. U. Kumar, C. Jacinto and D. Jaque, *Appl. Phys. Lett.*, 2016, **108**.
136. L. Marciniak, A. Pilch, S. Arabasz, D. Jin and A. Bednarkiewicz, *Nanoscale*, 2017.